JGR Atmospheres

RESEARCH ARTICLE
10.1029/2023JD039092

Key Points:

- Diurnal variations in $PM_{2.5}$ bulk components and organic tracers reflect diurnal cycles of sources
- Light absorption of water and methanol extracts of $PM_{2.5}$ exhibited a similar diurnal profile that followed changes in levoglucosan
- Short-term and high time-resolved data of organic tracers should be used for source apportionment to avoid misclassification

Supporting Information:

Supporting Information may be found in the online version of this article.

Correspondence to:

M. Xie,
mingjie.xie@nuist.edu.cn;
mingjie.xie@colorado.edu

Citation:

Feng, W., Wang, X., Shao, Z., Liao, H., Wang, Y., & Xie, M. (2023). Time-resolved measurements of $PM_{2.5}$ chemical composition and brown carbon absorption in Nanjing, East China: Diurnal variations and organic tracer-based PMF analysis. *Journal of Geophysical Research: Atmospheres*, *128*, e2023JD039092. https://doi.org/10.1029/2023JD039092

Received 16 APR 2023
Accepted 4 SEP 2023

Author Contributions:

Conceptualization: Mingjie Xie
Funding acquisition: Hong Liao, Yuhang Wang, Mingjie Xie
Investigation: Wei Feng, Xinyue Wang, Zhijuan Shao
Methodology: Zhijuan Shao, Mingjie Xie
Project Administration: Mingjie Xie
Supervision: Mingjie Xie
Visualization: Xinyue Wang
Writing – original draft: Wei Feng
Writing – review & editing: Hong Liao, Yuhang Wang, Mingjie Xie

Time-Resolved Measurements of $PM_{2.5}$ Chemical Composition and Brown Carbon Absorption in Nanjing, East China: Diurnal Variations and Organic Tracer-Based PMF Analysis

Wei Feng[1], Xinyue Wang[1], Zhijuan Shao[2], Hong Liao[1], Yuhang Wang[3], and Mingjie Xie[1]

[1]Jiangsu Key Laboratory of Atmospheric Environment Monitoring and Pollution Control, Collaborative Innovation Center of Atmospheric Environment and Equipment Technology, School of Environmental Science and Engineering, Nanjing University of Information Science & Technology, Nanjing, China, [2]School of Environment Science and Engineering, Suzhou University of Science and Technology Shihu Campus, Suzhou, China, [3]School of Earth and Atmospheric Sciences, Georgia Institute of Technology, Atlanta, GA, USA

Abstract To understand diurnal variations in $PM_{2.5}$ composition and aerosol extract absorption, $PM_{2.5}$ samples were collected at intervals of 2 hr from 8:00 to 20:00 and 6 hr from 20:00 to 8:00 (the next day) in northern Nanjing, China, during the winter and summer of 2019–2020 and analyzed for bulk components, organic tracers, and light absorption of water and methanol extracts—a proxy measure of brown carbon (BrC). Diurnal patterns of measured species reflected the influences of primary emissions and atmospheric processes. Light absorption coefficients of water ($Abs_{365,w}$) and methanol extracts ($Abs_{365,m}$) at 365 nm shared a similar diurnal profile peaking at 18:00–20:00, generally following changes in biomass burning tracers. However, $Abs_{365,w}$, $Abs_{365,m}$, and their normalizations to organic aerosols increased at 14:00–16:00, earlier than that of levoglucosan in the late afternoon, which was attributed to secondarily formed BrC. The methanol extracts showed a less drastic decrease in light absorption at night than the water extracts and elevated absorption efficiency during 2:00–8:00. This is due to the fact that the water-insoluble OC has a longer lifetime and stronger light absorption than the water-soluble OC. According to the source apportionment results solved by positive matrix factorization (PMF), biomass burning and secondary formation were the major BrC sources in northern Nanjing, with an average total relative contribution of about 90%. Compared to previous studies, diurnal source cycles were added to the PMF simulations in this work by using time-resolved speciation data, which avoided misclassification of BrC sources.

Plain Language Summary Light-absorbing organic carbon (OC), also known as "brown carbon", plays an important role in influencing the Earth's radiative balance. Filter samples of particulate matter with an aerodynamic diameter of less than 2.5 μm ($PM_{2.5}$) were collected at a resolution of 2 hr from 8:00 to 20:00 and a resolution of 6 hr from 20:00 to 8:00 (the next day) in northern Nanjing, China, during the winter and summer of 2019 and 2020. To understand the diurnal variations of BrC and its sources, each sample was analyzed for bulk components (OC, elemental carbon, and water-soluble ions), organic molecular markers, and light absorption by BrC, and a receptor model was used to identify potential BrC sources based on $PM_{2.5}$ composition data. We found that diurnal variations of BrC generally followed changes in concentrations of levoglucosan-a tracer of biomass burning; the increase in BrC absorption in the early afternoon was caused by secondary formation of BrC chromophores; biomass burning and secondary formation were the main sources of BrC. Time-resolved measurements of $PM_{2.5}$ components were rarely used to investigate the diurnal variations of BrC and its sources, which is very important for modeling the climate impact of BrC.

1. Introduction

Organic aerosols (OAs) account for a significant fraction (20%–90%) of fine particulate matter (PM; G. Chen et al., 2022) and have potential impacts on human health (Déméautis et al., 2023; Mauderly & Chow, 2008) and climate (Yli-Juuti et al., 2021). To develop effective strategies for PM pollution control, receptor models have been commonly used to apportion speciated PM to sources or atmospheric processes (Stanek et al., 2011). Due to the lack of representative source profiles in specific study locations, positive matrix factorization (PMF) has become one of the most frequently used tools for source apportionment (Hopke et al., 2020). It resolves sources based on differences in the concentration time series of PM components (Dall'Osto et al., 2013) and

requires source-specific tracers and a sufficient number of observations (Shrivastava et al., 2007; Y. X. Zhang et al., 2009). In the last 1–2 decades, hourly measurements of water-soluble inorganic ions (WSIIs), organic carbon (OC), elemental carbon (EC), and elements have been conducted and validated by offline observations (Yu et al., 2020, 2019). Compared with integrated sampling-based analysis, where PM collection typically takes 12–24 hr, high time-resolved observations had the advantage of reflecting the diurnal cycles of PM sources and capturing emerging pollution events that last only a few hours (Q. Wang et al., 2018; M. Xie et al., 2022a). Moreover, hourly measurements can generate enough observations required by the PMF model within a short time period (a few weeks to a month), mitigating the impact of assuming a constant source profile. Short-term observation-based PMF modeling is better able to reproduce immediate changes in primary sources than long-term observation-based modeling (Tian et al., 2017, 2020).

Speciation data of OA were usually obtained by integrated filter sampling followed by pretreatment and instrumental analysis (e.g., gas chromatography-mass spectrometry, GC-MS). Several classes of organic compounds, including *n*-alkanes, polycyclic aromatic hydrocarbons (PAHs), hopanes and steranes, polyols, polyacids, etc., have been identified and used for PMF analysis (Jaeckels et al., 2007; Shrivastava et al., 2007). Organic tracers have been shown to be preferred over elements in the identification of OA sources that do not have a unique elemental composition (Schauer et al., 1996; M. Xie et al., 2012b). The commercial thermal-desorption aerosol GC-MS has recently been used for hourly observations of organic molecular markers (OMMs) in eastern China (X. He et al., 2020; R. Li et al., 2020; Q. Wang et al., 2022). The observational results provide valuable information on the sources and evolution of primary and secondary organic aerosols (SOA) during pollution episodes. Unlike the aforementioned PM bulk components, hourly and filter-based measurements of OMMs have rarely been compared for validation.

The light absorption of OA in solvent extracts has been used to evaluate brown carbon (BrC) absorption (J. Liu et al., 2013), which plays an important role in changing the Earth's radiative equilibrium (Zeng et al., 2020). Hourly measurements of water-soluble OC (WSOC) absorption can be made by coupling a particle-in-liquid sampler with a UV-Vis spectrometer (Sullivan et al., 2022). Diurnal patterns of WSOC absorption in the southeastern United States indicate the formation of strong chromophores in the afternoon due to heterogeneous reactions or gas-particle partitioning of SOA (Hecobian et al., 2010). However, water-insoluble OC (WIOC) contributed to larger proportions of the total BrC absorption (Huang et al., 2020). Since methanol can extract OA more thoroughly than water, methanol-extractable OC (MEOC) in ambient and source particles have been intensively studied to understand the relationship between BrC composition and their optical properties (Tang et al., 2020; Yuan et al., 2020). However, automated continuous measurements of PM extracts in organic solvents have not yet been performed. Although low molecular weight PAHs (MW; ≤300 Da) and nitrophenol-like compounds (NPCs) have been identified as BrC chromophores and are ubiquitously present (Sun et al., 2021; Yuan et al., 2021), large molecules (MW > 500–1,000 Da) with unknown structures dominate BrC absorption (Di Lorenzo et al., 2017; Di Lorenzo & Young, 2016). To attribute BrC absorption to sources, solvent extract absorption of ambient OA was combined with its compositional data as input for PMF analysis (M. Xie et al., 2019; M. Xie et al., 2022b; Z. Xu et al., 2022). The study results indicate that biomass and coal combustion accounted for the largest fraction of solvent extract absorption during the cold season, and a significant fraction of BrC was formed by gas-phase, aqueous, and/or heterogeneous reactions.

In previous PMF analysis based on organic tracers, BrC absorption and speciated OA data were obtained by analyzing the same integrated filter samples. To ensure a sufficient number of observations, filter samples with low time resolution (12–24 hr) had to be collected for at least several months to a year. Then, the resulting factors or sources are likely biased due to the assumption of constant source profiles, and their diurnal profiles cannot be shown. Even if continuous measurements of BrC absorption and PM composition were available at the same site, the output data from different instruments might not provide physicochemical information of the same PM type because of differences in sampler design (e.g., inlet type, PM size cut, and flow rate; Chow et al., 2010; Solomon et al., 2003). In this study, time-resolved filter samples of PM with an aerodynamic diameter ≤2.5 μm ($PM_{2.5}$) were collected from 2019 to 2020 in winter and summer at a suburb in northern Nanjing, eastern China. The light absorption of WSOC and MEOC and the concentrations of WSIIs, OC, EC, and a series of OMMs were analyzed for each filter sample. PMF modeling was applied to identify the sources of $PM_{2.5}$ components and BrC absorption by incorporating pre-screened OMM data. The results of the study revealed the diurnal patterns of $PM_{2.5}$ components and BrC sources and illustrated the advantage of using time-resolved OMM data for source apportionment.

2. Methods

2.1. Sampling

Time-resolved $PM_{2.5}$ samples were collected on the rooftop of a seven-story library building at Nanjing University of Information Science and Technology (NUIST, 32.21°N, 118.71°E). Detailed information about the sampler and PM speciation was provided in our previous studies (Gou et al., 2021; Qin et al., 2021; Yang et al., 2021). Briefly, two identical side-by-side mid-volume samplers (samplers I and II, $PM_{2.5}$-PUF-300, Mingye Environmental, China) equipped with 2.5 μm cut-point impactors were deployed to collect time-resolved $PM_{2.5}$ alternately at a flow rate of 300 L min^{-1}. After passing through the impactor, $PM_{2.5}$ in the air stream was collected on a pre-beaked (550°C, 4 hr) quartz fiber filter (20.3 cm × 12.6 cm, Munktell Filter AB, Sweden). $PM_{2.5}$ was sampled at 2 hr intervals from 8:00 to 20:00 and 6 hr intervals from 20:00 to 8:00 (the next day), so that eight filter samples were obtained on each sampling day. Time-resolved sampling was conducted on 7 days in January 2019 and 8 days in January 2020; 24-day sampling was accomplished in both summer 2019 and summer 2020. Sampling date and time information can be found in Table S1 in Supporting Information S1. Figure S1 in Supporting Information S1 shows the average diurnal variation in ambient temperature (temp., °C) and relative humidity (RH, %) during each sampling period from 2019 to 2020. Twenty-six field blank samples were collected intermittently throughout the sampling campaign. All filter samples were stored at −20°C prior to chemical analysis.

2.2. Chemical Analysis

2.2.1. Bulk Components

One-fourth of each filter sample (~50 cm^2) was extracted in 40 mL ultrapure water (18.2 MΩ) and then filtered using a 25 mm diameter polytetrafluorethylene (PTFE) filter (0.22 μm pore size, Anpl Laboratory Technologies Inc., China). Cations (NH_4^+, K^+, Mg^{2+}, and Ca^{2+}) and anions (SO_4^{2-} and NO_3^-) in the aqueous extract were determined using ion chromatography (IC, ICS-3000 and ICS-2000, Dionex, United States). WSOC was measured with a total OC analyzer (TOC-L, Shimadzu, Japan). A punch area (~0.50 cm^2) of each filter sample was analyzed for the content of OC and EC using a thermo-optical carbon analyzer (DRI, 2001A, Atmoslytic, United States) following the protocol IMPROVE-A. Yang et al. (2021) performed parallel sampling with samplers I and II at the same site, and the collocated precision analysis showed an uncertainty fraction of approximately 10% for the concentrations of $PM_{2.5}$ mass and major components (NH_4^+, SO_4^{2-}, NO_3^-, OC, and EC).

2.2.2. Non-Polar and Polar OMMs

One-eighth of each filter sample (~25 cm^2) was cut into pieces and extracted twice (15 min each time) with ultrasound in dichloromethane (DCM). Prior to solvent extraction, 20 μL of an isotopically labeled PAH solution (naphthalene-d8, acenaphthene-d10, phenanthrene-d10, chrysene-d10, and perylene-d12 at a concentration of 10 ng μL^{-1} in DCM) was added to the sample pieces as internal standard (IS). The DCM extract of each sample was filtered, rotary evaporated, and blown down to around 200 μL for GC-MS analysis. An aliquot of 2 μL was injected in splitless mode, and the inlet temperature was set at 280°C. Non-polar OMMs, including *n*-alkanes, PAHs, oxygenated PAHs (oxy-PAHs), and steranes, were separated with an Agilent HP-5 ms capillary column (30 m × 0.25 mm × 0.25 μm) following a temperature program from 50°C (held for 3 min) to 325°C at a ramp of 30°C min^{-1} (10 min).

Another aliquot of each filter sample was spiked with the same IS solution and then sonicated in a 1:1 (v/v) methanol-DCM mixture. After filtration and rotary evaporation, the concentrated extract was blown off to dryness with nitrogen gas. Then 50 μL of N, O-bis(trimethylsilyl)trifluoroacetamide (BSTFA): trimethylchlorosilane (TMCS; 99:1) and 10 μL pyridine were added to the dried extract and reacted at 70°C for 3 hr, converting the carboxyl and alcohol groups to the corresponding trimethylsilyl esters and ethers. The resulting derivative solution was cooled and diluted with 340 μL of pure hexane for GC-MS analysis. Our target polar OMMs were separated using the same column (HP-5 ms) following a temperature program from 50°C (2 min) to 120°C at 3°C min^{-1} (0 min) and then to 300°C at 6°C min^{-1} (10 min).

In this study, all OMMs in the sample extracts were quantified by constructing six-point calibration curves using the IS method. Information on the organic species and their quantification standards can be found in Table S2 in Supporting Information S1. The quantification results of individual OMMs in the extracts were corrected using the median values of field blanks, and the concentrations of individual OMMs in ambient air were calculated

from their total mass and the air volume of each filter sample. More details on the speciation methods and quality assurance/control have been described in our previous studies (Gou et al., 2021; Qin et al., 2021; Yang et al., 2021).

2.3. Light Absorption Measurement

An aliquot (1–2 mL) of the filter extract in water mentioned in Section 2.2.1 was analyzed for light absorbance ($A_{\lambda,w}$) at λ = 200–900 nm with a UV/Vis spectrometer (UV-1900, Shimadzu Corporation), which was converted to light absorption coefficient ($Abs_{\lambda,w}$, Mm^{-1}) by

$$Abs_{\lambda,w} = (A_{\lambda,w} - A_{700,w}) \times \frac{V_l}{V_a \times L} \ln(10) \quad (1)$$

where $A_{700,w}$ is subtracted to address baseline drift, V_L (m^3) is the volume of water used for extraction, V_a (m^3) denotes the air volume of the extracted filter aliquot, L (0.01 m) is the cuvette path length, and the resulting $Abs_{\lambda,w}$ was converted from base-10 to the natural logarithm (Hecobian et al., 2010). To evaluate the light absorption per unit mass of WSOC, the solution mass absorption efficiency ($MAE_{\lambda,w}$, $m^2\ g^{-1}$ C) was calculated as follows

$$MAE_{\lambda,w} = \frac{Abs_{\lambda,w}}{C_{WSOC}} \quad (2)$$

where C_{WSOC} denotes ambient concentrations of WSOC (μg m^{-3}). Since WIOC shows stronger light absorption than WSOC at the same location (M. Xie et al., 2022b), one fourth of each filter sample was extracted in 12 mL methanol. After filtration, the light absorbance ($A_{\lambda,m}$), light absorption coefficient ($Abs_{\lambda,m}$, Mm^{-1}), and solution mass absorption efficiency ($MAE_{\lambda,m}$, $m^2\ g^{-1}C$) of the methanol extracts were determined in the same manner as those of the water extracts. MEOC concentrations were calculated by multiplying OC concentrations by the average extraction efficiency of methanol (82.4%) from M. Xie et al. (2022b). In this study, Abs_λ and MAE_λ of water and methanol extracts at 365 nm were reported to compare with previous studies. Owing to the short sampling interval (2 hr) during the day, the light absorbance of the sample extracts at >400 nm was mostly close to 0 and subject to large uncertainty. Therefore, the solution absorption Ångström exponent (Å), determined by regression of lg (Abs_λ) against lg (λ) over 300–550 nm, was not reported.

2.4. PMF Source Apportionment

PMF version 5.0 developed by the U.S. Environmental Protection Agency was utilized to determine sources of $PM_{2.5}$ components and aerosol extract absorption based on time-resolved speciation data. The PMF model presumes that concentrations of $PM_{2.5}$ components measured at a given receptor site are linearly contributed by a number of time-variant factors (or sources) and uses an uncertainty-weighted least squares approach to identify factor profiles and determine factor contributions from observations (M. Xie et al., 2013).

Throughout the sampling campaign, only one filter sample (15 January 2019, 2:00–8:00 a.m.) was omitted for PMF analysis due to power failure of the air-pump. Candidate input species were selected based on uniqueness of tracer sources, overall proportion (<20%) of missing values and measurements below detection limits (BDL), average signal-to-noise ratio (concentration/uncertainty; S/N > 3), and the physical interpretability of the output factor profiles. EC was not considered because of its high fraction (22.8%) of BDL values, particularly after February 2020, when stringent measures were taken to control COVID-19. Our targeted non-polar OMMs with vapor pressures ≤10^{-9} atm at 298.15 K ($p^{o,*}L$) are mainly (>75%) present in the particle phase (Gou et al., 2021). Due to the high water content of the aerosol in northern Nanjing, more than 80% of the polar OMMs were expected to be dissolved in the aerosol phase (Qin et al., 2021). To alleviate the impacts of the gas-particle partitioning process, non-polar OMMs with $p^{o,*}L$ much greater than 10^{-9} atm were also excluded (Table S2 in Supporting Information S1). Light non-polar OMMs in the ambient were mainly attributed to evaporation of crude oil and petroleum products, which accounted for an insignificant fraction (about 1%) of MEOC absorption (M. Xie et al., 2022b). The resulting whole data set (PMF_{whole}) contained 499 observations of 52 species, including six bulk species (NH_4^+, Ca^{2+}, SO_4^{2-}, NO_3^-, OC, and WSOC), 44 OMMs (Table S2 in Supporting Information S1), $Abs_{365,w}$, and $Abs_{365,m}$. To evaluate the impact of assuming a constant source profile on PMF modeling, PMF was applied to speciation data obtained in summer (PMF_{summer}, N = 382) but not to winter data because

of the limited number of observations (117) compared to input species. Preparation of uncertainty data sets and treatment of missing and BDL values are included in the Supplement (Text S1 in Supporting Information S1).

The PMF_{whole} and PMF_{summer} data sets were tested for 4- to 10-factor PMF solutions. The robustness of each base case solution was assessed using three error estimation methods of PMF 5.0, including bootstrapping (BS), displacement (DISP), and bootstrapping enhanced with DISP (BS-DISP). The final factor number was determined based on the interpretability of each base case solution, the change in Q/Q_{exp} with factor numbers, and robustness assessment results. Tables S3 and S4 in Supporting Information S1 summarize the error estimation diagnostics and Q/Q_{exp} values of the 4- to 10-factor solutions for PMF_{whole} and PMF_{summer}, respectively. More details on Q/Q_{exp} and robustness analysis are provided in the Supplement (Text S2 in Supporting Information S1).

3. Results and Discussion

3.1. Overview of the Measurement Results

Table 1 shows the statistics for the time-weighted averages of $PM_{2.5}$ bulk components, groups of non-polar and polar OMMs, Abs_{365} and MAE_{365} of water and methanol extracts on each sampling day. The calculation method for the time-weighted averages is provided in the Supplement (Text S3 in Supporting Information S1). Tables S5 and S6 in Supporting Information S1 list averages and ranges of concentrations for individual non-polar and polar OMM species. Among $PM_{2.5}$ bulk components, NO_3^- and SO_4^{2-} lead the average concentrations in winter (23.8 ± 8.77 μg m^{-3}, 2019; 27.8 ± 13.9 μg m^{-3}, 2020) and summer (8.92 ± 3.25 μg m^{-3}, 2019; 7.67 ± 2.92 μg m^{-3}, 2020), respectively, followed by OC and NH_4^+ (Table 1). Although NH_4NO_3 is subject to significant evaporative losses in summer due to high ambient temperature, average NO_3^- concentrations (6.56 ± 4.92 μg m^{-3}, 2019; 6.49 ± 5.24 μg m^{-3}, 2020) were not far below those of SO_4^{2-} and were comparable to observations at the same sampling site in summer 2019 based on 12 hr integrated sampling (6.67 ± 5.75 μg m^{-3}; Yang et al., 2021). Yang et al. (2021) observed a strong correlation ($r = 0.72$, $p < 0.05$) between NO_3^- and water-soluble organic nitrogen. The high NO_3^- concentrations in summer could be partially related to hydrolysis of secondarily formed organic nitrates (Morales et al., 2021; Y. Wang et al., 2021). Except for SO_4^{2-} and NO_3^-, all bulk components showed a decreasing trend from 2019 to 2020. This could be largely due to the "Three-year Action Plan for Cleaner Air" (2018–2020) of China's State Council. All bulk species exhibited strong seasonality with average concentrations higher in winter than in summer, which is consistent with previous studies and can be attributed to changes in primary emissions and their evolution, transport and dispersion of air pollutants, and changes in meteorology (e.g., temperature and planetary boundary layer height [PBLH]; Yang et al., 2021; Yu et al., 2020). The $PM_{2.5}$ mass can be well explained by WSIIs, OC, and EC in urban Nanjing (M. Xie et al., 2022a; Yu et al., 2020). In this study, the reconstructed $PM_{2.5}$ attained Class II limit (35 μg m^{-3}) of the Chinese National Ambient Air Quality Standards (NAAQS) in summer 2019 (30.3 ± 11.3 μg m^{-3}) and 2020 (25.9 ± 10.5 μg m^{-3}; Table 1). Besides pollution control policies, stringent measures for controlling the COVID-19 epidemics after February 2020 reduced emissions of $PM_{2.5}$ and its precursors substantially (Hu et al., 2022; Lu et al., 2021), which might be the main reason for the sharp decrease in reconstructed $PM_{2.5}$ levels in summer 2020. However, the secondary formation of NO_3^- and SO_4^{2-} was less affected compared to 2019. Since NO_3^- and SO_4^{2-} accounted for more than 50% of the reconstructed $PM_{2.5}$ levels, cutting NO_X and SO_2 emissions should be continued at the regional scale to alleviate $PM_{2.5}$ pollution in the future.

Except for biogenic SOA tracers, the average concentrations of all groups of non-polar and polar OMMs decreased from 2019 to 2020 (Table 1). The speciated SOA tracers in this work are primarily associated with photochemical oxidations of isoprene and α-pinene—two biogenic volatile organic compounds (VOCs; Claeys et al., 2004, 2007; Surratt et al., 2006; Szmigielski et al., 2007), while other OMMs are emitted mainly from primary sources, including biomass burning (Simoneit et al., 1999), fossil fuel combustion (Rogge et al., 1993a; Schauer et al., 1999), resuspended soil and dust (Rogge et al., 1993b; Simoneit et al., 2004), etc. Field measurements have shown the dependence of biogenic SOA formation on sulfate and NO_X (L. Xu et al., 2015; Y. Q. Zhang et al., 2019). From 2019 to 2020, isoprene- and α-pinene-derived SOA tracers showed less or even no decrease (Table 1), which might be partly ascribed to the fact that the average concentrations of SO_4^{2-} and NO_3^- did not show significant differences between 2019 and 2020 ($p > 0.05$). The average concentrations of n-alkanes, PAHs, oxy-PAHs, and biomass burning tracers are more than twice as high in winter as in summer (Table 1). Gou et al. (2021) found that more than 50% of the non-polar OMMs with $p^{o,*}L > 10^{-9}$ atm were present in the gas phase at the same sampling site. In this study, the n-alkanes, PAHs, and oxy-PAHs with $p^{o,*}L > 10^{-9}$ atm

Journal of Geophysical Research: Atmospheres
10.1029/2023JD039092

Table 1
Statistics for Time-Weighted Daily Averages of $PM_{2.5}$ Bulk Components (μg m^{-3}), Non-Polar and Polar Organic Molecular Markers (OMMs) (ng m^{-3}), Abs_{365} (Mm^{-1}) and MAE_{365} (m^2 $g^{-1}C$) of Water and Methanol Extracts

	2019-Winter		2019-Summer		2020-Winter		2020-Summer		Whole	
	Average ± Stdev[a]	Range	Average ± Stdev	Range	Average ± Stdev	Range	Average ± Stdev	Range	Average ± Stdev	Range
Bulk species										
NH_4^+	10.6 ± 3.46	4.66–15.0	3.54 ± 1.84	1.02–6.75	7.07 ± 2.33	3.93–9.87	3.14 ± 2.50	0.40–9.98	4.62 ± 3.38	0.40–15.0
K^+	1.40 ± 0.40	0.88–1.97	0.50 ± 0.42	0.026–1.70	0.69 ± 0.23	0.33–1.01	0.21 ± 0.089	0.069–0.41	0.51 ± 0.47	0.026–1.97
Mg^{2+}	0.20 ± 0.042	0.13–0.26	0.069 ± 0.049	0.0015–0.16	0.17 ± 0.20	0.065–0.66	0.046 ± 0.034	0.0022–0.13	0.093 ± 0.099	0.0015–0.66
Ca^{2+}	2.01 ± 0.90	1.12–3.29	1.10 ± 0.44	0.26–1.80	0.61 ± 0.18	0.32–0.85	0.56 ± 0.46	0.12–1.93	0.94 ± 0.66	0.12–3.29
SO_4^{2-}	13.8 ± 7.77	4.83–28.5	8.92 ± 3.25	3.57–15.3	13.6 ± 6.81	5.34–22.0	7.67 ± 2.92	2.31–13.6	9.57 ± 4.88	2.31–28.5
NO_3^-	23.8 ± 8.77	12.1–35.6	6.56 ± 4.92	1.26–17.6	27.8 ± 13.9	8.98–45.4	6.49 ± 5.24	1.28–19.3	11.1 ± 10.9	1.26–45.4
OC	13.4 ± 3.77	8.59–19.9	7.06 ± 1.90	3.89–10.6	8.43 ± 3.48	3.07–13.7	6.42 ± 1.80	3.62–9.67	7.69 ± 3.13	3.07–19.9
EC	4.89 ± 1.18	2.89–5.88	2.58 ± 0.66	1.48–4.46	2.47 ± 1.40	0.90–4.80	1.40 ± 1.08	0.31–4.14	2.37 ± 1.43	0.31–5.88
WSOC	7.64 ± 1.89	4.84–10.6	5.15 ± 1.24	3.20–7.45	6.92 ± 2.50	2.75–9.92	4.04 ± 1.32	2.15–6.83	5.23 ± 1.96	2.15–10.6
Reconstructed $PM_{2.5}$[b]	70.1 ± 20.3	39.9–98.3	30.3 ± 11.3	13.8–49.3	60.8 ± 27.0	26.8–95.9	25.9 ± 10.5	11.1–53.7	36.9 ± 21.7	11.1–98.3
Non-polar OMMs										
n-Alkanes	121 ± 42.5	64.3–198	45.2 ± 13.1	25.6–85.9	75.4 ± 29.0	22.7–112	27.7 ± 11.0	14.0–55.9	50.8 ± 35.1	14.0–198
PAHs	26.6 ± 11.7	15.2–49.4	6.29 ± 5.42	2.54–27.6	17.8 ± 8.82	5.91–31.3	4.29 ± 3.13	1.70–12.4	9.25 ± 9.64	1.70–49.4
Oxy-PAHs	10.0 ± 2.93	6.05–13.7	2.30 ± 1.11	1.29–5.33	5.09 ± 2.27	1.57–7.84	1.55 ± 0.67	0.59–3.49	3.23 ± 3.03	0.59–13.7
Steranes	1.43 ± 1.00	0.53–3.60	2.31 ± 1.24	0.60–4.96	0.98 ± 0.37	0.44–1.49	1.17 ± 0.47	0.39–2.31	1.61 ± 1.05	0.39–4.96
Polar OMMs										
Isoprene SOA	3.51 ± 1.71	1.62–6.66	42.8 ± 37.7	6.50–137	2.11 ± 1.18	0.88–3.95	62.7 ± 48.9	18.8–211	40.9 ± 44.2	0.88–211
α-Pinene SOA	17.5 ± 7.97	7.49–25.7	43.9 ± 15.6	9.25–79.4	14.4 ± 9.79	5.47–35.6	34.8 ± 25.4	8.76–103	33.8 ± 21.8	5.47–103
Biomass burning tracers	215 ± 116	105–457	34.7 ± 25.3	13.2–111	83.8 ± 36.6	26.5–147	21.1 ± 15.9	8.04–87.1	55.8 ± 73.5	8.04–457
Sugar alcohols	14.0 ± 5.72	7.91–24.9	24.0 ± 15.2	9.35–58.1	9.98 ± 2.92	5.59–14.8	18.7 ± 9.24	6.24–41.6	19.1 ± 12.0	5.60–58.1
Saccharides	28.9 ± 9.00	17.3–42.6	80.5 ± 54.8	22.6–227	17.9 ± 4.62	12.8–24.5	48.5 ± 28.2	12.3–121	54.6 ± 44.1	12.3–227
Light absorption										
$Abs_{365,w}$	8.02 ± 2.26	5.63–12.8	2.28 ± 0.91	1.28–4.69	5.18 ± 2.62	2.05–8.53	1.84 ± 0.47	1.21–2.99	3.12 ± 2.41	1.21–12.8
$Abs_{365,m}$	18.8 ± 6.57	9.97–30.8	6.00 ± 2.76	1.62–13.6	9.39 ± 3.34	4.48–14.1	3.38 ± 1.14	1.64–5.76	6.86 ± 5.54	1.62–30.8
$MAE_{365,w}$	1.06 ± 0.32	0.79–1.67	0.45 ± 0.15	0.25–0.74	0.73 ± 0.17	0.45–1.02	0.51 ± 0.16	0.34–1.00	0.58 ± 0.26	0.25–1.67
$MAE_{365,m}$	1.79 ± 0.19	1.45–2.03	1.08 ± 0.48	0.35–2.19	1.42 ± 0.26	1.07–1.81	0.67 ± 0.19	0.27–1.08	1.05 ± 0.50	0.27–2.19

[a]Standard deviation. [b]Sum of WSIIs, OC, and EC.

(e.g., *n*-C18 and PHE) exhibited stronger seasonality than less volatile species (e.g., *n*-C24 and BbkF, Table S5 in Supporting Information S1). Besides the enhanced combustion emissions and unfavorable meteorological conditions (e.g., decrease in boundary layer height) in winter, low ambient temperature could induce the transport of more volatile *n*-alkanes, PAHs, and oxy-PAHs from the gas to the particle phase (M. Xie et al., 2014). Moreover, photochemical degradation is an important loss mechanism for OA in the atmosphere, and OMM degradation is expected to be faster in the gas phase than in the condensed phase (Donahue et al., 2013; Hennigan et al., 2010; Rudich et al., 2007). Therefore, OMMs are subject to more depletion in summer due to the higher ambient temperature, which promotes evaporation of particle-phase OMMs, and stronger solar radiation.

Steranes and hopanes are commonly used to indicate lubricating oil combustion in source apportionment studies (Dutton et al., 2010; Gou et al., 2021; Shrivastava et al., 2007). Unlike other non-polar OMMs, their average concentrations were higher in summer than in winter (Table 1). Such seasonal variability was also observed in our previous studies in northern Nanjing (Gou et al., 2021) and urban Denver (M. Xie et al., 2012a). One possible explanation is that motor vehicle emissions increase during hot periods due to the lower density of intake air (L. W. A. Chen et al., 2001; Human et al., 1990). Biogenic SOA tracers showed an obvious elevation in summer (Table 1 and Table S6 in Supporting Information S1), which can be attributed to increased rates of biogenic emissions and photochemical reactions. The average total concentrations of biomass burning tracers were more than four times higher in winter (2019, 215 ± 116 ng m^{-3}; 2020, 83.8 ± 36.6 ng m^{-3}) than in summer (2019, 34.7 ± 25.3 ng m^{-3}; 2020, 21.1 ± 15.9 ng m^{-3}), indicating stronger biomass burning emissions from surrounding rural communities in winter. Sugar alcohols and saccharides are typical tracers of the soil microbiota (Simoneit et al., 2004). Their average concentrations increased significantly in summer (Table 1) due to high levels of vegetation (Verma et al., 2018; Yttri et al., 2007). Because biomass burning can also contribute to particulate saccharides and sugar alcohols (Marynowski & Simoneit, 2022), average concentrations of some species (e.g., pinitol) were comparable between summer and winter (Table S6 in Supporting Information S1).

Abs_{365} and MAE_{365} values of water and methanol extracts showed similar seasonal and year-to-year variations as WSOC and OC (Table 1). Owning to the drop in primary emissions (e.g., biomass and coal combustion) and increased photobleaching in summer (M. Xie et al., 2022b), aerosol extracts exhibited much higher light absorption in winter. As shown in Table 1, the average values of Abs_{365} (water/methanol extracts, 3.12 ± 2.41/6.86 ± 5.54 Mm^{-1}) and MAE_{365} (0.58 ± 0.26/1.06 ± 0.50 m^2 $g^{-1}C$) of the whole period are comparable with those obtained at the same site from 2018/2009 to 2019/2009 ($Abs_{365,w}$/$Abs_{365,m}$, 3.31 ± 2.19/7.88 ± 4.85 Mm^{-1}; $MAE_{365,w}$/$MAE_{365,m}$, 0.64 ± 0.28/1.16 ± 0.56 m^2 $g^{-1}C$) when integrated $PM_{2.5}$ samples were collected every sixth day (M. Xie et al., 2022b). The concentrations of OC and WSOC and their light absorption in aerosol extracts have been studied at the NUIST site since 2015 and showed a decreasing trend (D. Chen et al., 2019; X. Xie et al., 2020). More comparisons of Abs_{365} and MAE_{365} values across studies were provided in M. Xie et al. (2022b).

3.2. Diurnal Variations

3.2.1. Bulk Species

Diurnal variations of $PM_{2.5}$ bulk components during the whole period are visualized with box plots in Figure S2 in Supporting Information S1. Figure S3 in Supporting Information S1 exhibits the diurnal patterns of average concentrations of individual bulk species from winter 2019 to summer 2020. Concentrations of NH_4^+ correlated ($r > 0.65$, $p < 0.01$) with those of NO_3^- and SO_4^{2-} during each sampling period from 2019 to 2020, supporting the fact that NH_4^+ is primarily generated by neutralization reactions of NH_3 with secondarily formed HNO_3 and H_2SO_4 (Trebs et al., 2005). Thus, diurnal variations of NH_4^+ largely depend on NH_3 emissions and the formation of HNO_3 and H_2SO_4. In this study, the equivalent ratios of NH_4^+ to NO_3^- and SO_4^{2-} decreased continuously from winter 2019 (0.91 ± 0.21) to summer 2020 (0.54 ± 0.18), indicating a growing NH_4^+ deficit due to ammonia emission control in China (Dong et al., 2022; M. Liu et al., 2019). This is also an important reason for the alleviation of $PM_{2.5}$ pollution (Table 1). The diurnal pattern of SO_4^{2-} showed an increase from midday to early evening (Figures S2b and S3b in Supporting Information S1), which is ascribed to heterogeneous and aqueous oxidations of SO_2 (Cheng et al., 2016; G. Wang et al., 2016). Owning to the nighttime chemistry of NO_3 and N_2O_5 and the decrease in PBLH (H. Li et al., 2018; Pathak et al., 2011), a sharp increase in NO_3^- concentrations was observed at night in summer 2019 and 2020 (Figure S3c in Supporting Information S1). Besides soil crust, K^+ in $PM_{2.5}$ is also liked with biomass burning (Lee et al., 2016), and the difference in diurnal patterns between winter and summer (Figure S3d in Supporting Information S1) might reflect changes in primary sources. Both

Ca^{2+} and Mg^{2+} can be used as indicators of crustal dust (Krueger et al., 2004), and their concentrations showed a continuous decline from late afternoon to the morning of the next day (Figures S3e and S3f in Supporting Information S1). This is caused by the decrease in dust resuspension from traffic and construction activities during the night (Yu et al., 2020). OC originates from a mixture of primary emission sources and secondary formation pathways, and its median concentrations remain unchanged until the end of the first half of the night (Figure S2g in Supporting Information S1). The elevations of EC beginning at 8:00 and 18:00 reflected the influences of local traffic emissions (Figure S2h in Supporting Information S1). Unlike OC, WSOC showed a significant daytime increase of approximately 20% over the average nighttime concentration, indicating substantial photochemical SOA production, considering that PBLH rises from night to day (Hecobian et al., 2010).

3.2.2. Non-Polar and Polar OMMs

The average concentrations of individual OMM species during each sampling interval of the day for the entire period are summarized in Table S7 in Supporting Information S1. Figure 1 presents the diurnal variations of *n*-alkanes, PAHs, oxy-PAHs, and steranes during the whole period. To facilitate interspecies comparisons, *n*-alkanes, PAHs, and oxy-PAHs were grouped by their $p^{o,*}L$ values (Table S2 in Supporting Information S1), and the diurnal patterns of individual groups of non-polar OMMs are shown in Figure 1 and Figures S4–S6 in Supporting Information S1. Because the concentrations of *n*-alkanes, PAHs, and oxy-PAHs with $p^{o,*}L > 10^{-8}$ atm increased more dramatically from summer to winter than the less volatile species due to the gas-particle partitioning (Table S5 in Supporting Information S1), the day-night cycles of the non-polar OMMs largely depended on vapor pressure and ambient temperature. Our target steranes were supposed to exist mainly in the particle phase (Gou et al., 2021) and were not separated by vapor pressure. In Figures 1b, 1f, and 1j, the volatile *n*-alkanes, PAHs, and oxy-PAHs ($p^{o,*}L > 10^{-8}$ atm) show an increase in the morning (8:00–10:00) and late afternoon (16:00–18:00), reflecting the influences of motor vehicle emissions during rush hours. According to our previous studies, these low MW species were expected from unburned crude oil and petroleum products (Gou et al., 2021; M. Xie et al., 2022b).

Diurnal patterns of *n*-alkanes with $p^{o,*}L$ between 10^{-8} and 10^{-10} atm (carbon number 22–25) in summer 2019 and 2020 (Figure S4c in Supporting Information S1) were consistent with those of Ca^{2+} and Mg^{2+} (Figures S3e and S3f in Supporting Information S1), indicating diminished anthropogenic activities at night. These fossil fuel combustion-related species could be deposited on the land surface and mix with dust prior to entering the atmosphere through dust resuspension. Low-volatility *n*-alkanes ($p^{o,*}L < 10^{-10}$ atm) are contributed by a variety of sources, including tire wear debris in road dust (Rogge et al., 1993b), epicuticular plant waxes (Rogge et al., 1993c), cooking (L.-Y. He et al., 2004), etc. In Tables S5 and S7 in Supporting Information S1, the concentrations of *n*-C28 to *n*-C35 show a clear odd-to-even carbon number predominance across all sampling periods, indicating influences from biogenic emissions. However, the low-volatility *n*-alkanes exhibited weaker diurnal variability that changed across individual sampling periods (Figure S4d in Supporting Information S1), possibly due to variations in emission sources.

The influence of traffic on the concentrations of less volatile PAHs ($p^{o,*}L < 10^{-8}$ atm) during the late afternoon rush hour was observed only in winter (Figures S5c and S5d in Supporting Information S1), whereas their diurnal patterns in summer seem to be mainly shaped by the changes in PBLH. As shown in Figures S1 and S5 in Supporting Information S1, PAHs with $p^{o,*}L < 10^{-8}$ atm had the lowest concentrations at 14:00–16:00 in summer, when both ambient temperature and PBLH reached their diurnal maxima. In addition to the significant growth of PBLH from winter to summer (Y.-L. Zhang & Cao, 2015), increased photodegradation of PAHs might also contribute to the differences between winter and summer in their diurnal trends. Oxy-PAHs with $p^{o,*}L < 10^{-8}$ atm showed little increase during the afternoon rush hour (Figure 1k and Figure S6c in Supporting Information S1), indicating that traffic-related emissions are not a major source for these species. In contrast to low-volatility PAHs and oxy-PAHs, steranes presented higher average concentrations during the day (Table S7 in Supporting Information S1 and Figure 1l), particularly in summer when the highest concentrations occurred at 14:00–16:00 (Figure S6d in Supporting Information S1). This might be because steranes are primarily associated with motor vehicle emissions depending on ambient temperatures (L. W. A. Chen et al., 2001), and the steranes in deposited dust can re-enter the atmosphere through traffic-induced resuspension.

Figure S7 in Supporting Information S1 shows the diurnal variations of isoprene SOA products, α-pinene SOA products, biomass burning tracers, sugar alcohols, and saccharides in the whole period, and their average diurnal trends in each sampling period are provided in Figure 2. The isoprene SOA products consisted of 2-MG, three

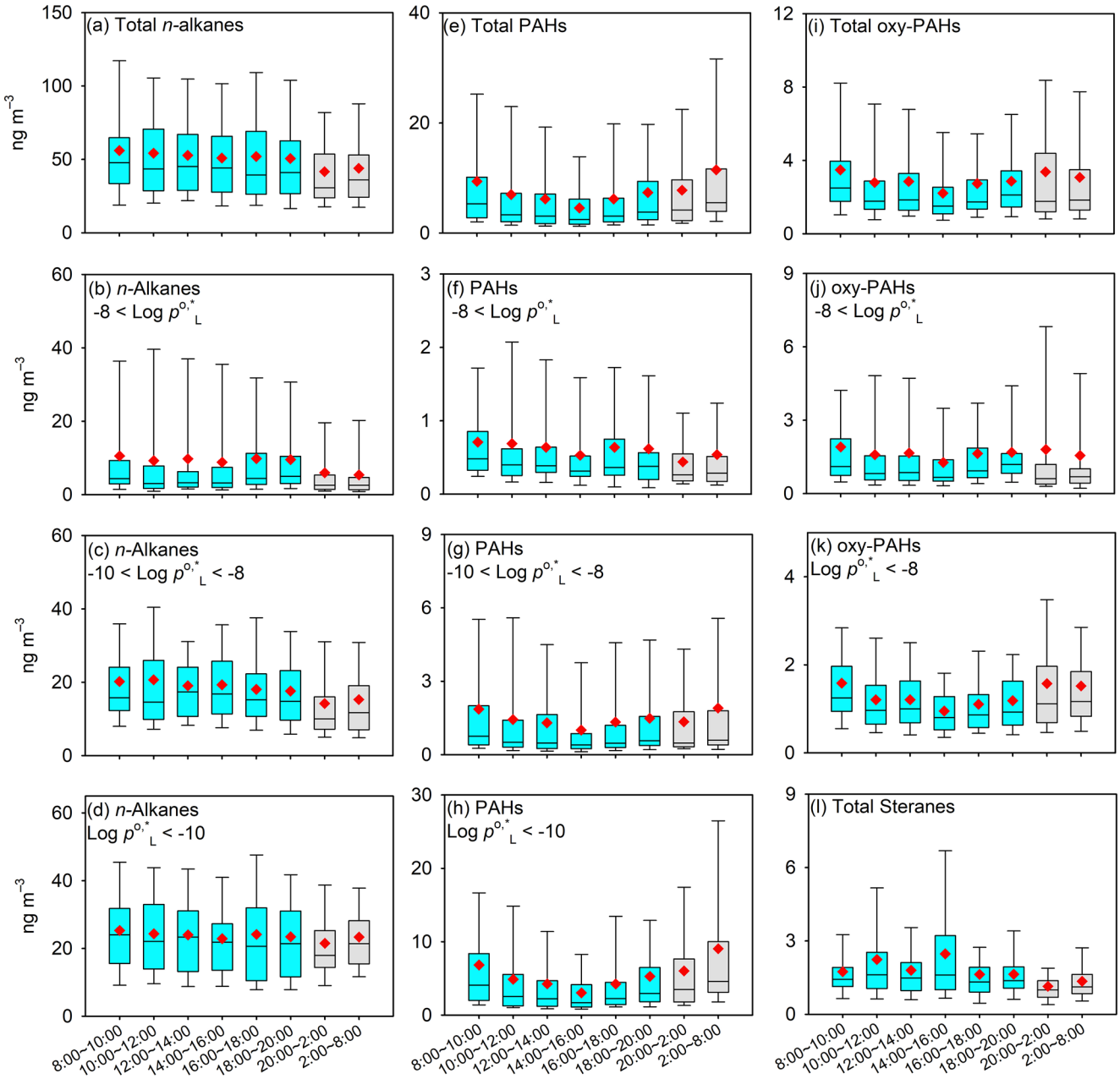

Figure 1. Diurnal variations of (a–d) *n*-alkanes, (e–h) polycyclic aromatic hydrocarbons (PAHs), and (i–k) oxy-PAHs in different vapor pressure ranges and (l) steranes during the whole period. The boxes depict the median (dark line), inner quartile (box), 10th and 90th percentiles (whiskers), and mean (red diamond). Cyan and gray boxes represent 2 hr (8:00–20:00) and 6 hr (20:00–8:00 the next day) sampling intervals, respectively.

C5-alkene triols (cis-MTB, 2-MTB, and trans-MTB), and two 2-mehtyltetrols (2-MT and 2-MET; Table S2 in Supporting Information S1). Their total concentrations increased from early morning and reached the maximum at 12:00–14:00 (Figure S7a in Supporting Information S1), which was caused by the photochemical oxidation of isoprene emitted mainly from deciduous trees. Such a diurnal pattern was observed for all six isoprene SOA tracers (Table S7 in Supporting Information S1), but these species had low levels and no clear diurnal trends in winter (Figure 2a). Biogenic contributions to airborne isoprene overwhelm anthropogenic counterparts at noon in summer, while biogenic emissions are no longer the dominant source of isoprene during the day in winter (Chang et al., 2014). In this study, 3-Methylbutane-1,2,3-tricarboxylic acid (MBTCA) and two hydroxyglutaric acids (2/3-HG) were measured to represent α-pinene SOA products. Because these species are later generation oxidation products (Claeys et al., 2007; Müller et al., 2012), their concentrations in summer increased from

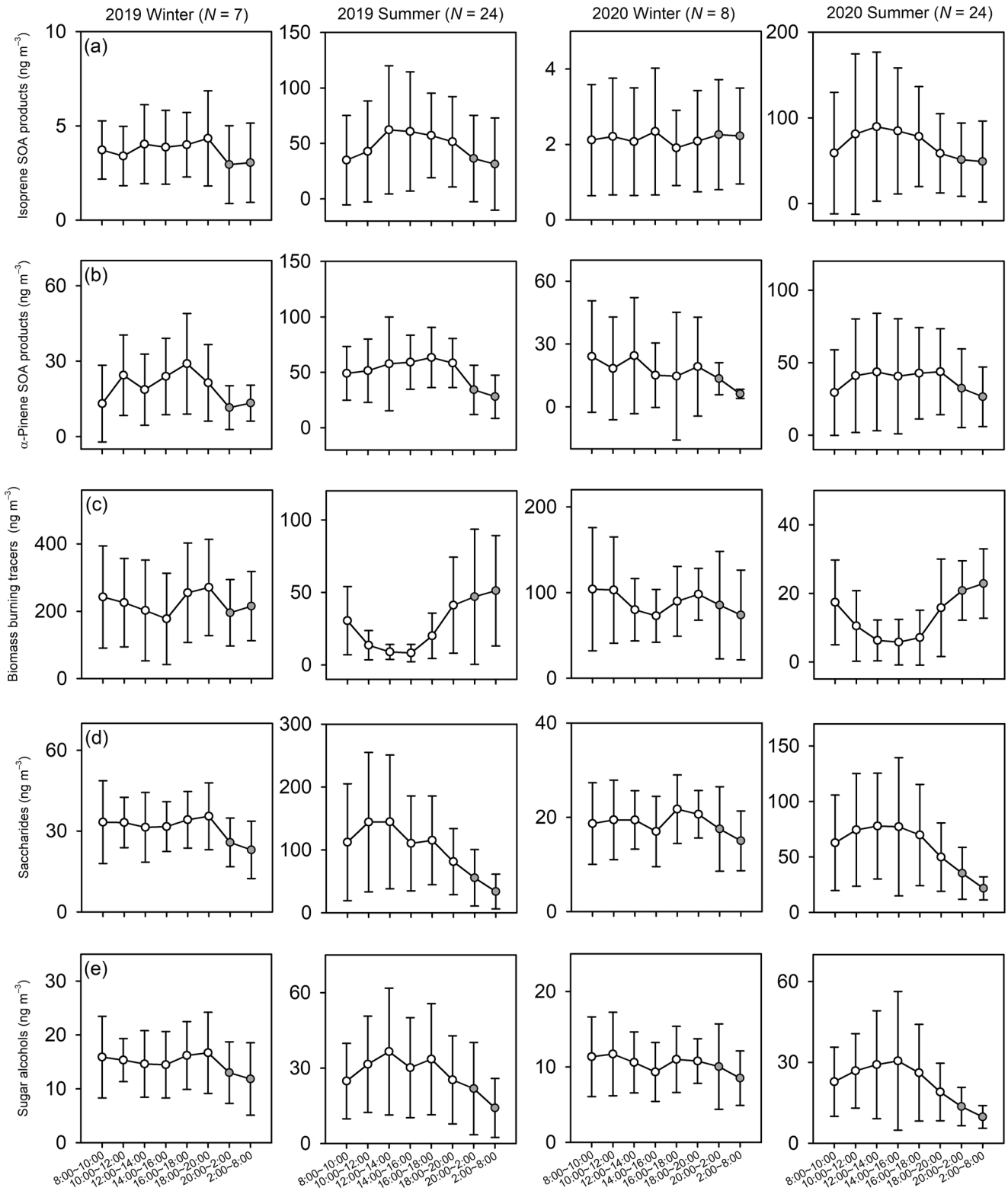

Figure 2. Average diurnal variations of (a) isoprene secondary organic aerosols (SOA) products, (b) α-pinene SOA products, (c) biomass burning tracers, (d) saccharides, and (e) sugar alcohols during each sampling period from 2019 to 2020. Blank and gray circles represent 2 and 6 hr sampling intervals, respectively, and the error bars denote ± one standard deviation.

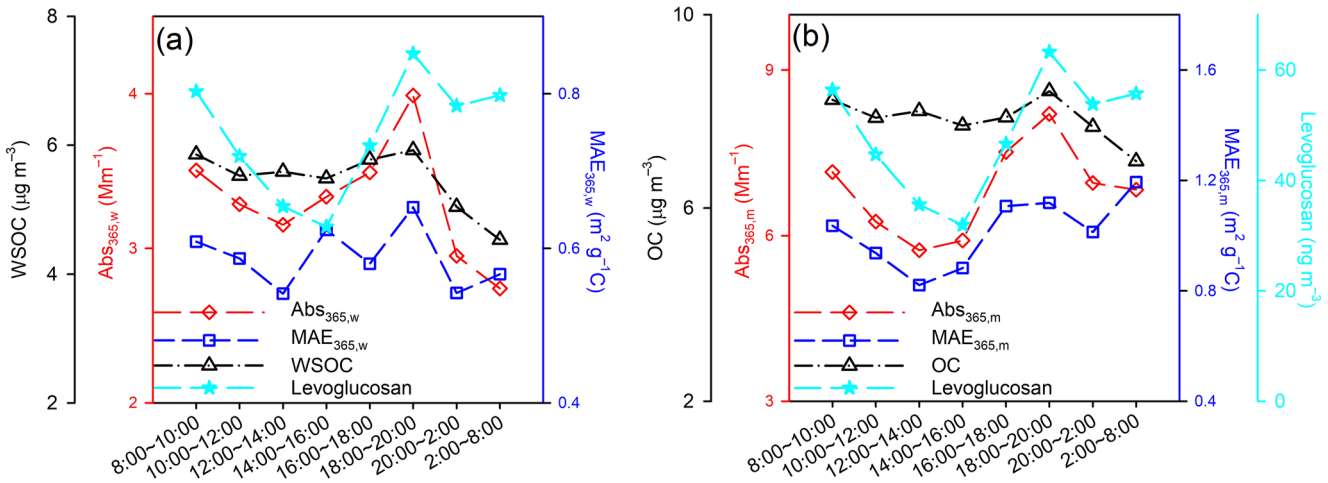

Figure 3. Mean diurnal profiles of Abs_{365} and MAE_{365} for (a) water-soluble OC (WSOC) and (b) methanol-extractable OC and associated $PM_{2.5}$ components.

morning until late afternoon and then decreased during the night (Figure 2b). Biomass burning can emit significant amounts of isoprene and terpenoids (Akagi et al., 2011; Andreae & Merlet, 2001), and significant correlations between biogenic SOA tracers and levoglucosan were observed in several field studies during biomass burning-influenced pollution episodes (Ding et al., 2016; J. Li et al., 2019). This might be a possible explanation for the difference in diurnal patterns of biogenic SOA products between winter and summer.

Levoglucosan was the most abundant species among the four biomass burning tracers (Tables S6 and S7 in Supporting Information S1). However, these species exhibited two distinct diurnal patterns in summer and winter (Figure 2c). Their total concentrations reached a minimum during the day in summer at 12:00–18:00 due to increased PBLH. The elevated levels in the morning (8:00–10:00) and late afternoon (16:00–20:00) in winter (Figure 2c) were attributed to biomass burning from local domestic heating activities (e.g., cooking). Sugar alcohols and saccharides are primarily associated with biological aerosol particles (e.g., soil microbiota, pollen, and fungal spores) and enriched in the coarse mode (Yttri et al., 2007). As shown in Figures 2d, 2e and Figures S7d, S7e in Supporting Information S1, both sugar alcohols and saccharides have daytime elevations in all sampling periods, and the modest increase from late afternoon to early evening in winter is likely caused by biomass burning emissions.

3.2.3. Light Absorption of WSOC and MEOC

Figure 3 shows the mean diurnal profiles of Abs_{365} and MAE_{365} during the whole period for WSOC and MEOC, and the measurement results of WSOC, OC, and levoglucosan are also included for comparison. The average diurnal variations of Abs_{365} and MAE_{365} for individual sampling periods are exhibited in Figure S8 in Supporting Information S1. Although average $Abs_{365,m}$ values were approximately twice as large as $Abs_{365,w}$ values throughout the measurement campaign (Table 1), both followed a nearly consistent diurnal trend that likely tracked biomass burning emissions (Figure 3).

Concentrations of levoglucosan and Abs_{365} values of WSOC and MEOC decreased more rapidly than WSOC and OC from 8:00 to 14:00, which was caused by the expansion of boundary layer and indicated that freshly formed SOA contains few light-absorbing chromophores (Hecobian et al., 2010). Moreover, chromophores emitted from primary sources (e.g., biomass burning and motor vehicles) in the morning are subject to "photobleaching" and evaporation as solar radiation and temperature increase (Satish et al., 2017; Zhong & Jang, 2014). This also resulted in a decrease in MAE_{365} values over the same period. In Figure 3, Abs_{365} and MAE_{365} values begin to increase at 14:00–16:00 when levoglucosan reaches its minimum and no increase in WSOC and OC is observed. Hecobian et al. (2010) attributed the increase in aqueous extract absorption before the afternoon rush hour to the heterogeneous conversion of WSOC to more light-absorbing materials and gas-particle partitioning of secondarily formed BrC chromophores (e.g., NPCs). Thereafter, levoglucosan and Abs_{365} increased significantly peaking at 18:00–20:00, while WSOC and OC showed minor elevations, indicating the influence of biomass burning and other primary combustion sources emitting chromophores with high absorption efficiency.

Unlike $Abs_{365,m}$, the average values of $Abs_{365,w}$ between 20:00 and 8:00 of the next day were lower than its minimum during the day. Because WSOC and OC concentrations decreased similarly during the night, $MAE_{365,m}$ exhibited a greater increase at 2:00–8:00 than $MAE_{365,w}$. Thus, we infer that water-soluble chromophores have a shorter lifetime than water-insoluble organics, resulting in a higher proportion of water-insoluble BrC with higher absorption efficiency during the nighttime. Among all OMM groups, biomass burning tracers had the strongest correlation with Abs_{365} ($r > 0.80$, $p < 0.01$), and the correlations of light absorption with WSOC ($r = 0.51$–0.88) and OC ($r = 0.54$–0.85) are stronger than with EC ($r = 0.18$–0.57) and low-volatility PAHs (0.14–0.52) across the four sampling periods. Therefore, biomass burning and SOA formation are supposed to be the main BrC sources dominating at different times of the day.

3.3. Source Apportionment

After testing 4- to 10-factor solutions for the PMF_{total} data set, Q/Q_{exp} decreased by 9.23% from 7 to 8 factors, which was less significant than the decrease from 4 to 7 factors (10.3%–12.4%). The six-factor solution of PMF_{total} failed to separate Ca^{2+} from steranes specifically related to different sources, whereas the error code of the eight-factor solution for DISP analysis (a nonzero value) indicated invalid results (Table S3 in Supporting Information S1). Finally, a seven-factor solution was selected because it provided the most interpretable source profiles (Figure 4). Because the output source information of the PMF_{total} solution was biased due to the changes in source profiles from winter to summer (M. Xie et al., 2022a), a seven-factor PMF_{summer} solution was determined for comparison. In Table S4 in Supporting Information S1, the change in Q/Q_{exp} slows down after the seven-factor solution (8.86%–10.6%). For the seven-factor PMF_{summer} solution, there was no factor swap during the DISP and BS-DISP analysis, and the source profiles matched those of the PMF_{total} solution (Figure 4). Moreover, good agreement was observed between input data and the PMF estimates of solvent extract absorption and bulk component concentrations (Table S8 in Supporting Information S1), suggesting that the seven-factor solution can properly reproduce the average and variations of the input species. Figure 5 and Figure S9 in Supporting Information S1 show the diurnal variations of stacked factor contributions to solvent extract absorption and input bulk species, respectively. According to the characteristic species of each factor and source profiles identified in our previous studies (M. Xie et al., 2022b; Z. Xu et al., 2022), the seven factors were related to biomass burning, secondary inorganics, biogenic SOA, dust resuspension, coal combustion, microbial activity, and lubricating oil combustion. The average relative contributions of these factors to $Abs_{365,w}$, $Abs_{365,m}$, and input bulk species are listed in Table S9 in Supporting Information S1.

The biomass burning factor was featured by the highest percentage of levoglucosan, and NH_4^+, SO_4^{2-}, and NO_3^- were mainly distributed to the secondary organics factor (Figures 4a and 4b). These two factors had comparable relative contributions to solvent extract absorption in winter and accounted for approximately 90% of the total (Table S9 in Supporting Information S1). The inclusion of isoprene-derived SOA tracers led to the identification of a biogenic SOA factor, but a larger fraction of SOA is produced with other precursors (e.g., anthropogenic VOCs) and mechanisms. Owning to the lack of relevant OMMs, substantial secondarily formed OAs, particularly anthropogenic SOA, and associated light absorption could be mixed with the secondary inorganics factor. This is because the PMF fits the input data and separates sources primarily based on the difference in temporal variability between input species (Dall'Osto et al., 2013; Shrivastava et al., 2007). From winter to summer, the relative contributions of biomass burning to $Abs_{365,m}$ showed little change, even when only summer data were analyzed, while the secondary inorganics factor had much lower relative contributions to $Abs_{365,w}$ (around 1/4), comparable to those of the biogenic SOA factor (Table S9 in Supporting Information S1). There is evidence that isoprene-related polymerization processes in the aerosol phase can generate light-absorbing chromophores (Lin et al., 2014; Nakayama et al., 2015), and the light-absorbing compounds in biogenic SOA are speculated to be aldol condensation oligomers formed in highly acidic aerosols (Nguyen et al., 2012; Song et al., 2013). In contrast to the biogenic SOA factor, the biomass burning and secondary inorganics factors showed lower contributions to WSOC and OC than to their light absorption in summer. This is due to the fact that biomass burning organics and anthropogenic SOA have higher absorption efficiency than biogenic SOA (M. Xie et al., 2017, 2019; M. Xie, Hays, & Holder, 2017).

In our previous studies where the speciation data of 12 hr integrated samples were analyzed, biomass burning showed similar contributions to $Abs_{365,w}$ (31.6%) and $Abs_{365,m}$ (48.0%) as in this work, while a significant fraction of carbonaceous aerosols and solvent extract absorption (>20%) were apportioned to the dust resuspension factor

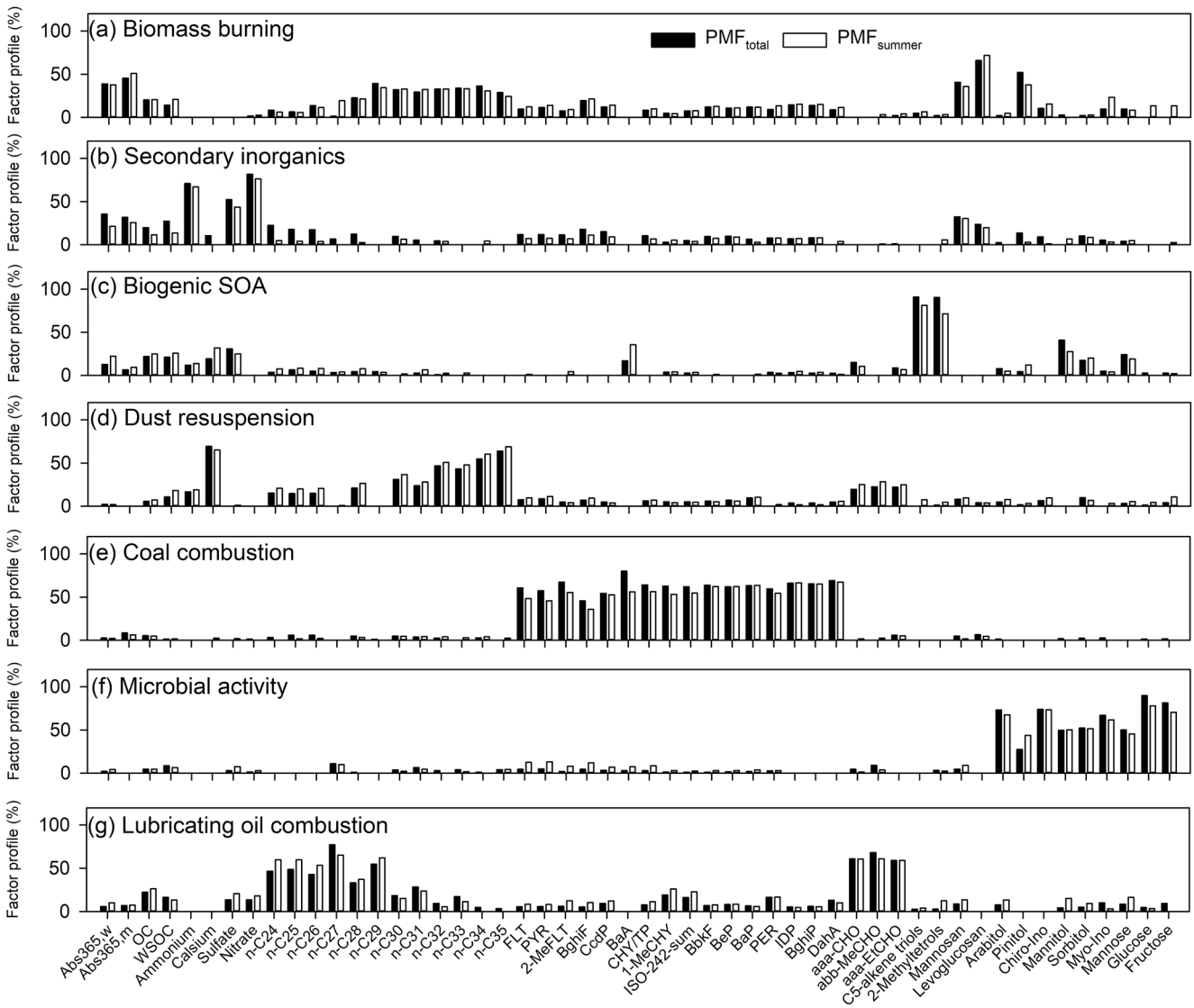

Figure 4. Comparisons of the normalized factor profiles between seven-factor PMF$_{total}$ and PMF$_{summer}$ solutions.

characterized by the highest loading of Ca^{2+} (M. Xie et al., 2022b; Z. Xu et al., 2022). As shown in Table 1, Figure S2 in Supporting Information S1, and Figure 3, both Ca^{2+} and solvent extract absorption exhibit an increase during the day and winter compared with the values during the night and summer, but the diurnal profiles of Ca^{2+} are distinct from those of $Abs_{365,w}$ and $Abs_{365,m}$. In this study, the dust resuspension factor contributed a very small fraction (<5%) of aerosol extract absorption. The misclassification of BrC sources based on low time-resolved measurements is likely caused by the missing of diurnal source cycles. The coal combustion, microbial activity, and lubricating oil combustion factors were identified and well explained at the same study location and were not major sources of BrC (Gou et al., 2021; M. Xie et al., 2022b; Z. Xu et al., 2022). The stacked factor contributions of the PMF$_{total}$ and PMF$_{summer}$ solutions reasonably reflected the diurnal patterns of input species (Figure 5 and Figure S9 in Supporting Information S1), but the peak values were usually underestimated. Because the PMF model operates under the non-negative constraint and requires that mean values be well fitted, it tends to overestimate small values and underestimate large values of input species (Henry & Christensen, 2010).

To evaluate the impacts of the identified sources on the temporal variations of $MAE_{365,w}$ and $MAE_{365,m}$, the contributions of individual factors to MAE_{365} were estimated by dividing their contributions to Abs_{365} by total factor contributions to solvent-extractable organics (WSOC or OC × 82.4%). As shown in Figure S10 in Supporting Information S1, biomass burning and secondary inorganics dominated factor contributions to $MAE_{365,w}$ and

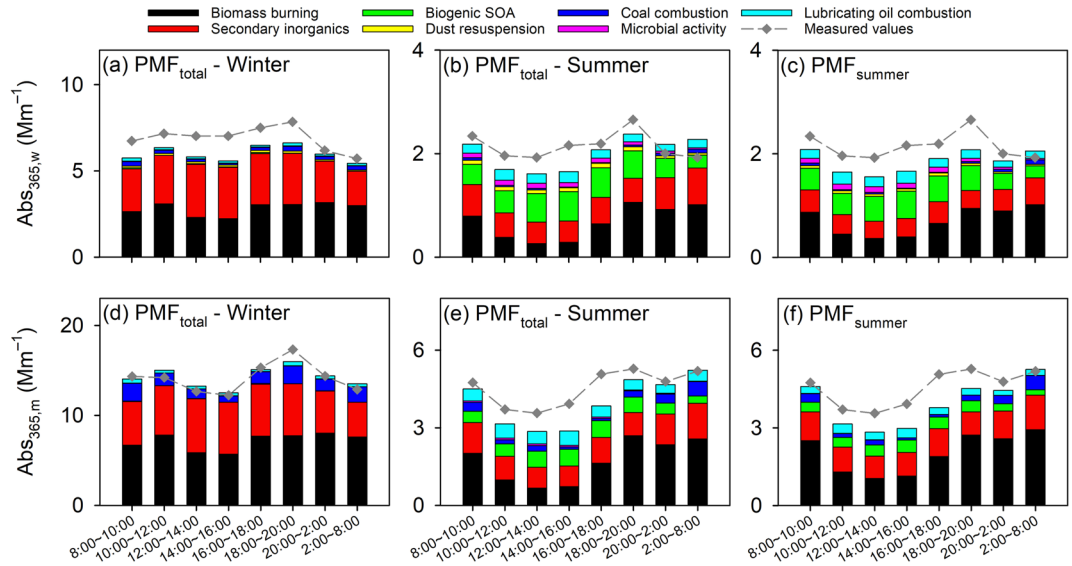

Figure 5. Diurnal distributions of factor contributions to (a–c) $Abs_{365,w}$ and (d–f) $Abs_{365,m}$ in winter and summer, derived from PMF_{total} and PMF_{summer} solutions.

$MAE_{365,m}$ in winter. The estimated diurnal variations of $MAE_{365,m}$ were consistent with the measured values in winter (Figure S10d in Supporting Information S1), which was attributed to the similarity between measured and estimated $Abs_{365,m}$ and OC (Figure 5d and Figure S9a in Supporting Information S1). Due to the underestimation of $Abs_{365,w}$ and overestimation of WSOC during the day in winter (Figure 5a and Figure S9d in Supporting Information S1), the total factor contributions to $MAE_{365,w}$ failed to reflect its increase from 14:00 to 20:00 and nighttime decrease (Figure S10a in Supporting Information S1). The estimates based on the PMF_{total} and PMF_{summer} solutions captured the decrease in $MAE_{365,w}$ and $MAE_{365,m}$ from 8:00 to 14:00 in summer (Figures S10b, S10c, S10e, and S10f in Supporting Information S1). This was directly related to the rapid decline in biomass burning contributions, which arrived their minimum at 12:00–16:00. In summer, the relative contributions of secondary inorganics and biogenic SOA to $MAE_{365,w}$ and $MAE_{365,m}$ began to increase from 10:00 and reached their maximum during 12:00–16:00 ($MAE_{365,w}$, >50%; $MAE_{365,m}$, >45%), supporting that the initial elevations in measured $MAE_{365,w}$ and $MAE_{365,m}$ at 14:00–16:00 were associated with secondarily formed light-absorbing materials. After 16:00, the relative contributions of biomass burning to $MAE_{365,w}$ and $MAE_{365,m}$ increased rapidly from <30% to >40% (PMF_{total} solution), which could lead to the increase of measured $MAE_{365,w}$ at 18:00–20:00 and upsurge in measured $MAE_{365,m}$ during 16:00–20:00. Figure S11 in Supporting Information S1 shows the seasonal distributions of factor contributions to $MAE_{365,w}$ and $MAE_{365,m}$ from 2019 to 2020, and PMF_{total} estimates generally reproduced the seasonal variations of $MAE_{365,w}$ and $MAE_{365,m}$. In comparison to 2019, the contributions of biomass burning to $MAE_{365,w}$ and $MAE_{365,m}$ decreased by more than 30% in both winter and summer, while total contributions from secondary inorganics and biogenic SOA increased. Since WIOC from biomass burning has stronger light absorption than WSOC, the increase in secondary BrC formation in summer 2020 might not offset the decreased contributions of $Abs_{365,m}$ from biomass burning. As shown in Table 1, average summertime $Abs_{365,m}$ decreased faster (43.7%) than $Abs_{365,w}$ (19.3%), OC (9.07%), and WSOC (21.6%) from 2019 to 2020. Therefore, the decrease in biomass burning activities was responsible for the significant annual changes in $Abs_{365,m}$ and $MAE_{365,m}$, and the increased secondary BrC formation balanced the effects of lower biomass burning on the annual changes of $MAE_{365,w}$.

In general, the PMF_{total} and PMF_{summer} solutions had similar factor profiles and factor contribution distributions for solvent extract absorption and most bulk species (Figures 4, 5, and Figure S9 in Supporting Information S1). However, a greater fraction of SO_4^{2-} was attributed to the biogenic SOA factor in the PMF_{total} solution in summer (46.1%) than in the PMF_{summer} solution (25.6%, Table S9 in Supporting Information S1). Both SO_4^{2-} and the input isoprene SOA tracers (C5-alkene triols and 2-methyltetrols) are secondary products in the atmosphere. Part of the input isoprene SOA tracers are present as organosulfates formed by the reactive uptake of isoprene epoxy diols and subsequent addition of inorganic sulfate or hydroxy sulfate ester (Cui et al., 2018; Surratt et al., 2010). As

shown in Figure 2a and Figure S3b in Supporting Information S1, SO_4^{2-} and isoprene SOA products have similar diurnal profiles, particularly in winter. In summer, peak concentrations of SO_4^{2-} occurred later than those of isoprene SOA products in the afternoon. Due to the pre-assumption of constant source profiles, a notable proportion of SO_4^{2-} could be misclassified into the biogenic SOA factor for the PMF_{total} solution in summer (Figure S9k in Supporting Information S1). Therefore, short-term and high time-resolved measurement data should be used to avoid unreasonable source apportionment results in the future.

4. Conclusions

In this work, time-resolved $PM_{2.5}$ samples were collected in northern Nanjing during the winter and summer of 2019 and 2020 and were analyzed for bulk components, OMMs, and solvent extract absorption. Except for SO_4^{2-}, NO_3^-, and biogenic SOA tracers, all other bulk components and primary source-related OMMs showed a decreasing trend from 2019 to 2020, and the average $PM_{2.5}$ concentration reconstructed by WSIIs, OC, and EC in summer 2020 (25.9 ± 10.5 μg m^{-3}) was more than 25% lower than the Class II limit (35 μg m^{-3}) of China's NAAQS, indicating a significant reduction of $PM_{2.5}$ emissions and precursors by the "Three-year Action Plan for Cleaner Air" and control measures for COVID-19 after February 2020. The Abs_{365} and MAE_{365} of aerosol extracts presented comparable values and similar seasonal variations to those in previous studies at the same location.

The diurnal variations of $PM_{2.5}$ bulk components were shaped by the combined influences of primary emissions, secondary formation, changes in PBLH, etc. Volatile *n*-alkanes, PAHs, and oxy-PAHs with $p^{o,*}L > 10^{-8}$ atm exhibited elevated concentrations at 8:00–10:00 and 16:00–18:00, reflecting evaporative emissions of fossil fuels during rush hours. Owning to the diversity in sources, the less volatile *n*-alkanes did not have a consistent diurnal pattern across the sampling periods. The day-night cycles of the less volatile PAHs and oxy-PAHs were more likely driven by changes in PBLH, particularly in summer. In contrast to other non-polar OMMs, steranes had increased concentrations in summer. Their diurnal profiles indicated more contributions from dust resuspension than direct combustion sources. The concentration peak of α-pinene SOA products appeared later (16:00–18:00) than that of isoprene SOA products (12:00–14:00) as the measured α-pinene tracers are later generation oxidation products. Biomass burning tracers showed peak concentrations from 16:00 to 20:00 only in winter, which can be attributed to emissions from domestic heating activities in the surrounding rural areas. Sugar alcohols and saccharides originated mainly from biological aerosol particles and showed prominent daytime elevations.

The mean diurnal profiles of $Abs_{365,m}$ and $Abs_{365,w}$ followed the changes in the mean concentrations of biomass burning tracers, and the earlier increase in MAE_{365} at 14:00–16:00 compared with levoglucosan indicated the secondary formation of light-absorbing materials. The source apportionment results showed that biomass burning and secondary formation dominated the light absorption of aerosol extract absorption. The decline in $MAE_{365,m}$ from 2019 to 2020 was primarily ascribed to the decrease in biomass burning activities. In our previous studies, 12 hr integrated sample data were used for PMF analysis, and a considerable fraction of aerosol extract absorption was misclassified into the dust resuspension factor due to the lack of diurnal source cycles. This and the difference between the PMF_{total} and PMF_{summer} solutions suggest the use of short-term high-time resolved speciation data to avoid biased source apportionment results.

Conflict of Interest

The authors declare no conflicts of interest relevant to this study.

Data Availability Statement

Data used in the writing of this paper (and its Supporting Information file) are publicly available on Harvard Dataverse (Feng et al., 2023; https://doi.org/10.7910/DVN/ZN0G2S).

Acknowledgments
This work was supported by the National Natural Science Foundation of China (NSFC, 42177211).

References

Akagi, S. K., Yokelson, R. J., Wiedinmyer, C., Alvarado, M. J., Reid, J. S., Karl, T., et al. (2011). Emission factors for open and domestic biomass burning for use in atmospheric models. *Atmospheric Chemistry and Physics*, *11*(9), 4039–4072. https://doi.org/10.5194/acp-11-4039-2011

Andreae, M. O., & Merlet, P. (2001). Emission of trace gases and aerosols from biomass burning. *Global Biogeochemical Cycles*, *15*(4), 955–966. https://doi.org/10.1029/2000GB001382

Chang, C.-C., Wang, J.-L., Candice Lung, S.-C., Chang, C.-Y., Lee, P.-J., Chew, C., et al. (2014). Seasonal characteristics of biogenic and anthropogenic isoprene in tropical–subtropical urban environments. *Atmospheric Environment*, *99*, 298–308. https://doi.org/10.1016/j.atmosenv.2014.09.019

Chen, D., Zhao, Y., Lyu, R., Wu, R., Dai, L., Zhao, Y., et al. (2019). Seasonal and spatial variations of optical properties of light absorbing carbon and its influencing factors in a typical polluted city in Yangtze River Delta, China. *Atmospheric Environment*, *199*, 45–54. https://doi.org/10.1016/j.atmosenv.2018.11.022

Chen, G., Canonaco, F., Tobler, A., Aas, W., Alastuey, A., Allan, J., et al. (2022). European aerosol phenomenology—8: Harmonised source apportionment of organic aerosol using 22 year-long ACSM/AMS datasets. *Environment International*, *166*, 107325. https://doi.org/10.1016/j.envint.2022.107325

Chen, L. W. A., Doddridge, B. G., Dickerson, R. R., Chow, J. C., Mueller, P. K., Quinn, J., & Butler, W. A. (2001). Seasonal variations in elemental carbon aerosol, carbon monoxide and sulfur dioxide: Implications for sources. *Geophysical Research Letters*, *28*(9), 1711–1714. https://doi.org/10.1029/2000GL012354

Cheng, Y., Zheng, G., Wei, C., Mu, Q., Zheng, B., Wang, Z., et al. (2016). Reactive nitrogen chemistry in aerosol water as a source of sulfate during haze events in China. *Science Advances*, *2*(12), e1601530. https://doi.org/10.1126/sciadv.1601530

Chow, J. C., Watson, J. G., Chen, L. W. A., Rice, J., & Frank, N. H. (2010). Quantification of $PM_{2.5}$ organic carbon sampling artifacts in US networks. *Atmospheric Chemistry and Physics*, *10*(12), 5223–5239. https://doi.org/10.5194/acp-10-5223-2010

Claeys, M., Graham, B., Vas, G., Wang, W., Vermeylen, R., Pashynska, V., et al. (2004). Formation of secondary organic aerosols through photooxidation of isoprene. *Science*, *303*(5661), 1173–1176. https://doi.org/10.1126/science.1092805

Claeys, M., Szmigielski, R., Kourtchev, I., Van der Veken, P., Vermeylen, R., Maenhaut, W., et al. (2007). Hydroxydicarboxylic acids: Markers for secondary organic aerosol from the photooxidation of α-pinene. *Environmental Science & Technology*, *41*(5), 1628–1634. https://doi.org/10.1021/es0620181

Cui, T., Zeng, Z., dos Santos, E. O., Zhang, Z., Chen, Y., Zhang, Y., et al. (2018). Development of a hydrophilic interaction liquid chromatography (HILIC) method for the chemical characterization of water-soluble isoprene epoxydiol (IEPOX)-derived secondary organic aerosol. *Environmental Science: Processes & Impacts*, *20*(11), 1524–1536. https://doi.org/10.1039/C8EM00308D

Dall'Osto, M., Querol, X., Amato, F., Karanasiou, A., Lucarelli, F., Nava, S., et al. (2013). Hourly elemental concentrations in $PM_{2.5}$ aerosols sampled simultaneously at urban background and road site during SAPUSS—Diurnal variations and PMF receptor modelling. *Atmospheric Chemistry and Physics*, *13*(8), 4375–4392. https://doi.org/10.5194/acp-13-4375-2013

Déméautis, T., Bouyssi, A., Chapalain, A., Guillemot, J., Doublet, P., Geloen, A., et al. (2023). Chronic exposure to secondary organic aerosols causes lung tissue damage. *Environmental Science & Technology*, *57*(15), 6085–6094. https://doi.org/10.1021/acs.est.2c08753

Di Lorenzo, R. A., Washenfelder, R. A., Attwood, A. R., Guo, H., Xu, L., Ng, N. L., et al. (2017). Molecular-size-separated brown carbon absorption for biomass-burning aerosol at multiple field sites. *Environmental Science & Technology*, *51*(6), 3128–3137. https://doi.org/10.1021/acs.est.6b06160

Di Lorenzo, R. A., & Young, C. J. (2016). Size separation method for absorption characterization in brown carbon: Application to an aged biomass burning sample. *Geophysical Research Letters*, *43*(1), 458–465. https://doi.org/10.1002/2015GL066954

Ding, X., He, Q.-F., Shen, R.-Q., Yu, Q.-Q., Zhang, Y.-Q., Xin, J.-Y., et al. (2016). Spatial and seasonal variations of isoprene secondary organic aerosol in China: Significant impact of biomass burning during winter. *Scientific Reports*, *6*(1), 20411. https://doi.org/10.1038/srep20411

Donahue, N. M., Chuang, W., Epstein, S. A., Kroll, J. H., Worsnop, D. R., Robinson, A. L., et al. (2013). Why do organic aerosols exist? Understanding aerosol lifetimes using the two-dimensional volatility basis set. *Environmental Chemistry*, *10*(3), 151–157. https://doi.org/10.1071/EN13022

Dong, Z., Xing, J., Wang, S., Ding, D., Ge, X., Zheng, H., et al. (2022). Responses of nitrogen and sulfur deposition to NH_3 emission control in the Yangtze River Delta, China. *Environmental Pollution*, *308*, 119646. https://doi.org/10.1016/j.envpol.2022.119646

Dutton, S. J., Vedal, S., Piedrahita, R., Milford, J. B., Miller, S. L., & Hannigan, M. P. (2010). Source apportionment using positive matrix factorization on daily measurements of inorganic and organic speciated $PM_{2.5}$. *Atmospheric Environment*, *44*(23), 2731–2741. https://doi.org/10.1016/j.atmosenv.2010.04.038

Feng, W., Wang, X., Shao, Z., Liao, H., Wang, Y., Xie, M. (2023). Replication data for: Time-resolved measurements of $PM_{2.5}$ chemical composition and brown carbon absorption in Nanjing, East China: Diurnal variations and organic tracer-based PMF analysis (Version 2). *Harvard Dataverse*. https://doi.org/10.7910/DVN/ZN0G2S

Gou, Y., Qin, C., Liao, H., & Xie, M. (2021). Measurements, gas/particle partitioning, and sources of nonpolar organic molecular markers at a suburban site in the west Yangtze River Delta, China. *Journal of Geophysical Research: Atmospheres*, *126*(19), e2020JD034080. https://doi.org/10.1029/2020JD034080

He, L.-Y., Hu, M., Huang, X.-F., Yu, B.-D., Zhang, Y.-H., & Liu, D.-Q. (2004). Measurement of emissions of fine particulate organic matter from Chinese cooking. *Atmospheric Environment*, *38*(38), 6557–6564. https://doi.org/10.1016/j.atmosenv.2004.08.034

He, X., Wang, Q., Huang, X. H. H., Huang, D. D., Zhou, M., Qiao, L., et al. (2020). Hourly measurements of organic molecular markers in urban Shanghai, China: Observation of enhanced formation of secondary organic aerosol during particulate matter episodic periods. *Atmospheric Environment*, *240*, 117807. https://doi.org/10.1016/j.atmosenv.2020.117807

Hecobian, A., Zhang, X., Zheng, M., Frank, N., Edgerton, E. S., & Weber, R. J. (2010). Water-soluble organic aerosol material and the light-absorption characteristics of aqueous extracts measured over the Southeastern United States. *Atmospheric Chemistry and Physics*, *10*(13), 5965–5977. https://doi.org/10.5194/acp-10-5965-2010

Hennigan, C. J., Sullivan, A. P., Collett, J. L., & Robinson, A. L. (2010). Levoglucosan stability in biomass burning particles exposed to hydroxyl radicals. *Geophysical Research Letters*, *37*(9), L09806. https://doi.org/10.1029/2010GL043088

Henry, R. C., & Christensen, E. R. (2010). Selecting an appropriate multivariate source apportionment model result. *Environmental Science & Technology*, *44*(7), 2474–2481. https://doi.org/10.1021/es9018095

Hopke, P. K., Dai, Q., Li, L., & Feng, Y. (2020). Global review of recent source apportionments for airborne particulate matter. *Science of the Total Environment*, *740*, 140091. https://doi.org/10.1016/j.scitotenv.2020.140091

Hu, R., Wang, S., Zheng, H., Zhao, B., Liang, C., Chang, X., et al. (2022). Variations and sources of organic aerosol in winter Beijing under markedly reduced anthropogenic activities during COVID-2019. *Environmental Science & Technology*, *56*(11), 6956–6967. https://doi.org/10.1021/acs.est.1c05125

Huang, R.-J., Yang, L., Shen, J., Yuan, W., Gong, Y., Guo, J., et al. (2020). Water-insoluble organics dominate brown carbon in wintertime urban aerosol of China: Chemical characteristics and optical properties. *Environmental Science & Technology*, *54*(13), 7836–7847. https://doi.org/10.1021/acs.est.0c01149

Human, D. M., Ullman, T. L., & Baines, T. M. (1990). Simulation of high altitude effects on heavy-duty diesel emissions. *SAE Transactions*, *99*, 1791–1800. https://www.jstor.org/stable/44548192

Jaeckels, J. M., Bae, M. S., & Schauer, J. J. (2007). Positive matrix factorization (PMF) analysis of molecular marker measurements to quantify the sources of organic aerosols. *Environmental Science & Technology*, *41*(16), 5763–5769. https://doi.org/10.1021/es062536b

Krueger, B. J., Grassian, V. H., Cowin, J. P., & Laskin, A. (2004). Heterogeneous chemistry of individual mineral dust particles from different dust source regions: The importance of particle mineralogy. *Atmospheric Environment*, *38*(36), 6253–6261. https://doi.org/10.1016/j.atmosenv.2004.07.010

Lee, A. K. Y., Willis, M. D., Healy, R. M., Wang, J. M., Jeong, C. H., Wenger, J. C., et al. (2016). Single-particle characterization of biomass burning organic aerosol (BBOA): Evidence for non-uniform mixing of high molecular weight organics and potassium. *Atmospheric Chemistry and Physics*, *16*(9), 5561–5572. https://doi.org/10.5194/acp-16-5561-2016

Li, H., Zhang, Q., Zheng, B., Chen, C., Wu, N., Guo, H., et al. (2018). Nitrate-driven urban haze pollution during summertime over the North China Plain. *Atmospheric Chemistry and Physics*, *18*(8), 5293–5306. https://doi.org/10.5194/acp-18-5293-2018

Li, J., Wang, G., Zhang, Q., Li, J., Wu, C., Jiang, W., et al. (2019). Molecular characteristics and diurnal variations of organic aerosols at a rural site in the North China Plain with implications for the influence of regional biomass burning. *Atmospheric Chemistry and Physics*, *19*(16), 10481–10496. https://doi.org/10.5194/acp-19-10481-2019

Li, R., Wang, Q., He, X., Zhu, S., Zhang, K., Duan, Y., et al. (2020). Source apportionment of $PM_{2.5}$ in Shanghai based on hourly organic molecular markers and other source tracers. *Atmospheric Chemistry and Physics*, *20*(20), 12047–12061. https://doi.org/10.5194/acp-20-12047-2020

Lin, Y.-H., Budisulistiorini, S. H., Chu, K., Siejack, R. A., Zhang, H., Riva, M., et al. (2014). Light-absorbing oligomer formation in secondary organic aerosol from reactive uptake of isoprene epoxydiols. *Environmental Science & Technology*, *48*(20), 12012–12021. https://doi.org/10.1021/es503142b

Liu, J., Bergin, M., Guo, H., King, L., Kotra, N., Edgerton, E., & Weber, R. J. (2013). Size-resolved measurements of brown carbon in water and methanol extracts and estimates of their contribution to ambient fine-particle light absorption. *Atmospheric Chemistry and Physics*, *13*(24), 12389–12404. https://doi.org/10.5194/acp-13-12389-2013

Liu, M., Huang, X., Song, Y., Tang, J., Cao, J., Zhang, X., et al. (2019). Ammonia emission control in China would mitigate haze pollution and nitrogen deposition, but worsen acid rain. *Proceedings of the National Academy of Sciences of the United States of America*, *116*(16), 7760–7765. https://doi.org/10.1073/pnas.1814880116

Lu, D., Zhang, J., Xue, C., Zuo, P., Chen, Z., Zhang, L., et al. (2021). COVID-19-induced lockdowns indicate the short-term control effect of air pollutant emission in 174 cities in China. *Environmental Science & Technology*, *55*(7), 4094–4102. https://doi.org/10.1021/acs.est.0c07170

Marynowski, L., & Simoneit, B. R. T. (2022). Saccharides in atmospheric particulate and sedimentary organic matter: Status overview and future perspectives. *Chemosphere*, *288*, 132376. https://doi.org/10.1016/j.chemosphere.2021.132376

Mauderly, J. L., & Chow, J. C. (2008). Health effects of organic aerosols. *Inhalation Toxicology*, *20*(3), 257–288. https://doi.org/10.1080/08958370701866008

Morales, A. C., Jayarathne, T., Slade, J. H., Laskin, A., & Shepson, P. B. (2021). The production and hydrolysis of organic nitrates from OH radical oxidation of β-ocimene. *Atmospheric Chemistry and Physics*, *21*(1), 129–145. https://doi.org/10.5194/acp-21-129-2021

Müller, L., Reinnig, M. C., Naumann, K. H., Saathoff, H., Mentel, T. F., Donahue, N. M., & Hoffmann, T. (2012). Formation of 3-methyl-1,2,3-butanetricarboxylic acid via gas phase oxidation of pinonic acid—A mass spectrometric study of SOA aging. *Atmospheric Chemistry and Physics*, *12*(3), 1483–1496. https://doi.org/10.5194/acp-12-1483-2012

Nakayama, T., Sato, K., Tsuge, M., Imamura, T., & Matsumi, Y. (2015). Complex refractive index of secondary organic aerosol generated from isoprene/NO_x photooxidation in the presence and absence of SO_2. *Journal of Geophysical Research: Atmospheres*, *120*(15), 7777–7787. https://doi.org/10.1002/2015JD023522

Nguyen, T. B., Lee, P. B., Updyke, K. M., Bones, D. L., Laskin, J., Laskin, A., & Nizkorodov, S. A. (2012). Formation of nitrogen- and sulfur-containing light-absorbing compounds accelerated by evaporation of water from secondary organic aerosols. *Journal of Geophysical Research: Atmospheres*, *117*(D1), D01207. https://doi.org/10.1029/2011JD016944

Pathak, R. K., Wang, T., & Wu, W. S. (2011). Nighttime enhancement of $PM_{2.5}$ nitrate in ammonia-poor atmospheric conditions in Beijing and Shanghai: Plausible contributions of heterogeneous hydrolysis of N_2O_5 and HNO_3 partitioning. *Atmospheric Environment*, *45*(5), 1183–1191. https://doi.org/10.1016/j.atmosenv.2010.09.003

Qin, C., Gou, Y., Wang, Y., Mao, Y., Liao, H., Wang, Q., & Xie, M. (2021). Gas-particle partitioning of polyol tracers at a suburban site in Nanjing, East China: Increased partitioning to the particle phase. *Atmospheric Chemistry and Physics*, *21*(15), 12141–12153. https://doi.org/10.5194/acp-21-12141-2021

Rogge, W. F., Hildemann, L. M., Mazurek, M. A., Cass, G. R., & Simoneit, B. R. T. (1993a). Sources of fine organic aerosol. 2. Noncatalyst and catalyst-equipped automobiles and heavy-duty diesel trucks. *Environmental Science & Technology*, *27*(4), 636–651. https://doi.org/10.1021/es00041a007

Rogge, W. F., Hildemann, L. M., Mazurek, M. A., Cass, G. R., & Simoneit, B. R. T. (1993b). Sources of fine organic aerosol. 3. Road dust, tire debris, and organometallic brake lining dust—Roads as sources and sinks. *Environmental Science & Technology*, *27*(9), 1892–1904. https://doi.org/10.1021/es00046a019

Rogge, W. F., Hildemann, L. M., Mazurek, M. A., Cass, G. R., & Simoneit, B. R. T. (1993c). Sources of fine organic aerosol .4. Particulate abrasion products from leaf surfaces of urban plants. *Environmental Science & Technology*, *27*(13), 2700–2711. https://doi.org/10.1021/es00049a008

Rudich, Y., Donahue, N. M., & Mentel, T. F. (2007). Aging of organic aerosol: Bridging the gap between laboratory and field studies. *Annual Review of Physical Chemistry*, *58*(1), 321–352. https://doi.org/10.1146/annurev.physchem.58.032806.104432

Satish, R., Shamjad, P., Thamban, N., Tripathi, S., & Rastogi, N. (2017). Temporal characteristics of brown carbon over the central Indo-Gangetic Plain. *Environmental Science & Technology*, *51*(12), 6765–6772. https://doi.org/10.1021/acs.est.7b00734

Schauer, J. J., Kleeman, M. J., Cass, G. R., & Simoneit, B. R. T. (1999). Measurement of emissions from air pollution sources. 2. C_1 through C_{30} organic compounds from medium duty diesel trucks. *Environmental Science & Technology*, *33*(10), 1578–1587. https://doi.org/10.1021/es980081n

Schauer, J. J., Rogge, W. F., Hildemann, L. M., Mazurek, M. A., Cass, G. R., & Simoneit, B. R. (1996). Source apportionment of airborne particulate matter using organic compounds as tracers. *Atmospheric Environment*, *30*(22), 3837–3855. https://doi.org/10.1016/1352-2310(96)00085-4

Shrivastava, M. K., Subramanian, R., Rogge, W. F., & Robinson, A. L. (2007). Sources of organic aerosol: Positive matrix factorization of molecular marker data and comparison of results from different source apportionment models. *Atmospheric Environment*, *41*(40), 9353–9369. https://doi.org/10.1016/j.atmosenv.2007.09.016

Simoneit, B. R. T., Elias, V. O., Kobayashi, M., Kawamura, K., Rushdi, A. I., Medeiros, P. M., et al. (2004). Sugars dominant water-soluble organic compounds in soils and characterization as tracers in atmospheric particulate matter. *Environmental Science & Technology*, *38*(22), 5939–5949. https://doi.org/10.1021/es0403099

Simoneit, B. R. T., Schauer, J. J., Nolte, C. G., Oros, D. R., Elias, V. O., Fraser, M. P., et al. (1999). Levoglucosan, a tracer for cellulose in biomass burning and atmospheric particles. *Atmospheric Environment*, *33*(2), 173–182. https://doi.org/10.1016/S1352-2310(98)00145-9

Solomon, P., Baumann, K., Edgerton, E., Tanner, R., Eatough, D., Modey, W., et al. (2003). Comparison of integrated samplers for mass and composition during the 1999 Atlanta Supersites project. *Journal of Geophysical Research: Atmospheres*, *108*(D7), 8423. https://doi.org/10.1029/2001JD001218

Song, C., Gyawali, M., Zaveri, R. A., Shilling, J. E., & Arnott, W. P. (2013). Light absorption by secondary organic aerosol from α-pinene: Effects of oxidants, seed aerosol acidity, and relative humidity. *Journal of Geophysical Research: Atmospheres*, *118*(20), 11741–11749. https://doi.org/10.1002/jgrd.50767

Stanek, L. W., Sacks, J. D., Dutton, S. J., & Dubois, J.-J. B. (2011). Attributing health effects to apportioned components and sources of particulate matter: An evaluation of collective results. *Atmospheric Environment*, *45*(32), 5655–5663. https://doi.org/10.1016/j.atmosenv.2011.07.023

Sullivan, A. P., Pokhrel, R. P., Shen, Y., Murphy, S. M., Toohey, D. W., Campos, T., et al. (2022). Examination of brown carbon absorption from wildfires in the western US during the WE-CAN study. *Atmospheric Chemistry and Physics*, *22*(20), 13389–13406. https://doi.org/10.5194/acp-22-13389-2022

Sun, Y., Tang, J., Mo, Y., Geng, X., Zhong, G., Yi, X., et al. (2021). Polycyclic aromatic carbon: A key fraction determining the light absorption properties of methanol-soluble brown carbon of open biomass burning aerosols. *Environmental Science & Technology*, *55*(23), 15724–15733. https://doi.org/10.1021/acs.est.1c06460

Surratt, J. D., Chan, A. W. H., Eddingsaas, N. C., Chan, M., Loza, C. L., Kwan, A. J., et al. (2010). Reactive intermediates revealed in secondary organic aerosol formation from isoprene. *Proceedings of the National Academy of Sciences of the United States of America*, *107*(15), 6640–6645. https://doi.org/10.1073/pnas.0911114107

Surratt, J. D., Murphy, S. M., Kroll, J. H., Ng, N. L., Hildebrandt, L., Sorooshian, A., et al. (2006). Chemical composition of secondary organic aerosol formed from the photooxidation of isoprene. *The Journal of Physical Chemistry A*, *110*(31), 9665–9690. https://doi.org/10.1021/jp061734m

Szmigielski, R., Surratt, J. D., Gómez-González, Y., Van der Veken, P., Kourtchev, I., Vermeylen, R., et al. (2007). 3-methyl-1,2,3-butanetricarboxylic acid: An atmospheric tracer for terpene secondary organic aerosol. *Geophysical Research Letters*, *34*(24), L24811. https://doi.org/10.1029/2007GL031338

Tang, J., Li, J., Su, T., Han, Y., Mo, Y., Jiang, H., et al. (2020). Molecular compositions and optical properties of dissolved brown carbon in biomass burning, coal combustion, and vehicle emission aerosols illuminated by excitation-emission matrix spectroscopy and Fourier transform ion cyclotron resonance mass spectrometry analysis. *Atmospheric Chemistry and Physics*, *20*(4), 2513–2532. https://doi.org/10.5194/acp-20-2513-2020

Tian, Y., Xiao, Z., Wang, H., Peng, X., Guan, L., Huangfu, Y., et al. (2017). Influence of the sampling period and time resolution on the PM source apportionment: Study based on the high time-resolution data and long-term daily data. *Atmospheric Environment*, *165*, 301–309. https://doi.org/10.1016/j.atmosenv.2017.07.003

Tian, Y., Zhang, Y., Liang, Y., Niu, Z., Xue, Q., & Feng, Y. (2020). $PM_{2.5}$ source apportionment during severe haze episodes in a Chinese megacity based on a 5-month period by using hourly species measurements: Explore how to better conduct PMF during haze episodes. *Atmospheric Environment*, *224*, 117364. https://doi.org/10.1016/j.atmosenv.2020.117364

Trebs, I., Metzger, S., Meixner, F. X., Helas, G., Hoffer, A., Rudich, Y., et al. (2005). The NH_4^+-NO_3^--Cl^--SO_4^{2-}-H_2O aerosol system and its gas phase precursors at a pasture site in the Amazon Basin: How relevant are mineral cations and soluble organic acids? *Journal of Geophysical Research: Atmospheres*, *110*(D7), D07303. https://doi.org/10.1029/2004JD005478

Verma, S. K., Kawamura, K., Chen, J., & Fu, P. (2018). Thirteen years of observations on primary sugars and sugar alcohols over remote Chichijima Island in the western North Pacific. *Atmospheric Chemistry and Physics*, *18*(1), 81–101. https://doi.org/10.5194/acp-18-81-2018

Wang, G., Zhang, R., Gomez, M. E., Yang, L., Levy Zamora, M., Hu, M., et al. (2016). Persistent sulfate formation from London Fog to Chinese haze. *Proceedings of the National Academy of Sciences of the United States of America*, *113*(48), 13630–13635. https://doi.org/10.1073/pnas.1616540113

Wang, Q., Qiao, L., Zhou, M., Zhu, S., Griffith, S., Li, L., & Yu, J. Z. (2018). Source apportionment of $PM_{2.5}$ using hourly measurements of elemental tracers and major constituents in an urban environment: Investigation of time-resolution influence. *Journal of Geophysical Research: Atmospheres*, *123*(10), 5284–5300. https://doi.org/10.1029/2017JD027877

Wang, Q., Wang, S., Cheng, Y. Y., Chen, H., Zhang, Z., Li, J., et al. (2022). Chemical evolution of secondary organic aerosol tracers during high-$PM_{2.5}$ episodes at a suburban site in Hong Kong over 4 months of continuous measurement. *Atmospheric Chemistry and Physics*, *22*(17), 11239–11253. https://doi.org/10.5194/acp-22-11239-2022

Wang, Y., Piletic, I. R., Takeuchi, M., Xu, T., France, S., & Ng, N. L. (2021). Synthesis and hydrolysis of atmospherically relevant monoterpene-derived organic nitrates. *Environmental Science & Technology*, *55*(21), 14595–14606. https://doi.org/10.1021/acs.est.1c05310

Xie, M., Chen, X., Hays, M. D., Lewandowski, M., Offenberg, J., Kleindienst, T. E., & Holder, A. L. (2017). Light absorption of secondary organic aerosol: Composition and contribution of nitroaromatic compounds. *Environmental Science & Technology*, *51*(20), 11607–11616. https://doi.org/10.1021/acs.est.7b03263

Xie, M., Chen, X., Holder, A. L., Hays, M. D., Lewandowski, M., Offenberg, J. H., et al. (2019). Light absorption of organic carbon and its sources at a southeastern U.S. location in summer. *Environmental Pollution*, *244*, 38–46. https://doi.org/10.1016/j.envpol.2018.09.125

Xie, M., Coons, T. L., Dutton, S. J., Milford, J. B., Miller, S. L., Peel, J. L., et al. (2012a). Intra-urban spatial variability of $PM_{2.5}$-bound carbonaceous components. *Atmospheric Environment*, *60*, 486–494. https://doi.org/10.1016/j.atmosenv.2012.05.041

Xie, M., Hannigan, M. P., & Barsanti, K. C. (2014). Gas/particle partitioning of *n*-alkanes, PAHs and oxygenated PAHs in urban Denver. *Atmospheric Environment*, *95*, 355–362. https://doi.org/10.1016/j.atmosenv.2014.06.056

Xie, M., Hannigan, M. P., Dutton, S. J., Milford, J. B., Hemann, J. G., Miller, S. L., et al. (2012b). Positive matrix factorization of $PM_{2.5}$: Comparison and implications of using different speciation data sets. *Environmental Science & Technology*, *46*(21), 11962–11970. https://doi.org/10.1021/es302358g

Xie, M., Hays, M. D., & Holder, A. L. (2017). Light-absorbing organic carbon from prescribed and laboratory biomass burning and gasoline vehicle emissions. *Scientific Reports*, *7*(1), 7318. https://doi.org/10.1038/s41598-017-06981-8

Xie, M., Lu, X., Ding, F., Cui, W., Zhang, Y., & Feng, W. (2022a). Evaluating the influence of constant source profile presumption on PMF analysis of $PM_{2.5}$ by comparing long- and short-term hourly observation-based modeling. *Environmental Pollution*, *314*, 120273. https://doi.org/10.1016/j.envpol.2022.120273

Xie, M., Peng, X., Shang, Y., Yang, L., Zhang, Y., Wang, Y., & Liao, H. (2022b). Collocated measurements of light-absorbing organic carbon in $PM_{2.5}$: Observation uncertainty and organic tracer-based source apportionment. *Journal of Geophysical Research: Atmospheres*, *127*(5), e2021JD035874. https://doi.org/10.1029/2021JD035874

Xie, M., Piedrahita, R., Dutton, S. J., Milford, J. B., Hemann, J. G., Peel, J. L., et al. (2013). Positive matrix factorization of a 32-month series of daily $PM_{2.5}$ speciation data with incorporation of temperature stratification. *Atmospheric Environment*, *65*, 11–20. https://doi.org/10.1016/j.atmosenv.2012.09.034

Xie, X., Chen, Y., Nie, D., Liu, Y., Liu, Y., Lei, R., et al. (2020). Light-absorbing and fluorescent properties of atmospheric brown carbon: A case study in Nanjing, China. *Chemosphere*, *251*, 126350. https://doi.org/10.1016/j.chemosphere.2020.126350

Xu, L., Guo, H., Boyd, C. M., Klein, M., Bougiatioti, A., Cerully, K. M., et al. (2015). Effects of anthropogenic emissions on aerosol formation from isoprene and monoterpenes in the southeastern United States. *Proceedings of the National Academy of Sciences of the United States of America*, *112*(1), 37–42. https://doi.org/10.1073/pnas.1417609112

Xu, Z., Feng, W., Wang, Y., Ye, H., Wang, Y., Liao, H., & Xie, M. (2022). Potential underestimation of ambient brown carbon absorption based on the methanol extraction method and its impacts on source analysis. *Atmospheric Chemistry and Physics*, *22*(20), 13739–13752. https://doi.org/10.5194/acp-22-13739-2022

Yang, L., Shang, Y., Hannigan, M. P., Zhu, R., Wang, Q. g., Qin, C., & Xie, M. (2021). Collocated speciation of $PM_{2.5}$ using tandem quartz filters in northern Nanjing, China: Sampling artifacts and measurement uncertainty. *Atmospheric Environment*, *246*, 118066. https://doi.org/10.1016/j.atmosenv.2020.118066

Yli-Juuti, T., Mielonen, T., Heikkinen, L., Arola, A., Ehn, M., Isokääntä, S., et al. (2021). Significance of the organic aerosol driven climate feedback in the boreal area. *Nature Communications*, *12*(1), 5637. https://doi.org/10.1038/s41467-021-25850-7

Yttri, K. E., Dye, C., & Kiss, G. (2007). Ambient aerosol concentrations of sugars and sugar-alcohols at four different sites in Norway. *Atmospheric Chemistry and Physics*, *7*(16), 4267–4279. https://doi.org/10.5194/acp-7-4267-2007

Yu, Y., Ding, F., Mu, Y., Xie, M., & Wang, Q. g. (2020). High time-resolved $PM_{2.5}$ composition and sources at an urban site in Yangtze River Delta, China after the implementation of the APPCAP. *Chemosphere*, *261*, 127746. https://doi.org/10.1016/j.chemosphere.2020.127746

Yu, Y., He, S., Wu, X., Zhang, C., Yao, Y., Liao, H., et al. (2019). $PM_{2.5}$ elements at an urban site in Yangtze River Delta, China: High time-resolved measurement and the application in source apportionment. *Environmental Pollution*, *253*, 1089–1099. https://doi.org/10.1016/j.envpol.2019.07.096

Yuan, W., Huang, R. J., Yang, L., Guo, J., Chen, Z., Duan, J., et al. (2020). Characterization of the light-absorbing properties, chromophore composition and sources of brown carbon aerosol in Xi'an, northwestern China. *Atmospheric Chemistry and Physics*, *20*(8), 5129–5144. https://doi.org/10.5194/acp-20-5129-2020

Yuan, W., Huang, R. J., Yang, L., Wang, T., Duan, J., Guo, J., et al. (2021). Measurement report: $PM_{2.5}$-bound nitrated aromatic compounds in Xi'an, Northwest China—Seasonal variations and contributions to optical properties of brown carbon. *Atmospheric Chemistry and Physics*, *21*(5), 3685–3697. https://doi.org/10.5194/acp-21-3685-2021

Zeng, L., Zhang, A., Wang, Y., Wagner, N. L., Katich, J. M., Schwarz, J. P., et al. (2020). Global measurements of brown carbon and estimated direct radiative effects. *Geophysical Research Letters*, *47*(13), e2020GL088747. https://doi.org/10.1029/2020GL088747

Zhang, Y.-L., & Cao, F. (2015). Fine particulate matter ($PM_{2.5}$) in China at a city level. *Scientific Reports*, *5*(1), 14884. https://doi.org/10.1038/srep14884

Zhang, Y. Q., Chen, D. H., Ding, X., Li, J., Zhang, T., Wang, J. Q., et al. (2019). Impact of anthropogenic emissions on biogenic secondary organic aerosol: Observation in the Pearl River Delta, southern China. *Atmospheric Chemistry and Physics*, *19*(22), 14403–14415. https://doi.org/10.5194/acp-19-14403-2019

Zhang, Y. X., Sheesley, R. J., Bae, M. S., & Schauer, J. J. (2009). Sensitivity of a molecular marker based positive matrix factorization model to the number of receptor observations. *Atmospheric Environment*, *43*(32), 4951–4958. https://doi.org/10.1016/j.atmosenv.2009.07.009

Zhong, M., & Jang, M. (2014). Dynamic light absorption of biomass-burning organic carbon photochemically aged under natural sunlight. *Atmospheric Chemistry and Physics*, *14*(3), 1517–1525. https://doi.org/10.5194/acp-14-1517-2014

References From the Supporting Information

Brown, S. G., Eberly, S., Paatero, P., & Norris, G. A. (2015). Methods for estimating uncertainty in PMF solutions: Examples with ambient air and water quality data and guidance on reporting PMF results. *Science of the Total Environment*, *518–519*, 626–635. https://doi.org/10.1016/j.scitotenv.2015.01.022

Norris, G., Duvall, R., Brown, S., Bai, S. J. I., & Petaluma (2014). *EPA positive matrix factorization (PMF) 5.0 fundamentals and user guide prepared for the US environmental protection*. Agency Office of Research and Development.

Paatero, P., Eberly, S., Brown, S., & Norris, G. (2014). Methods for estimating uncertainty in factor analytic solutions. *Atmospheric Measurement Techniques*, *7*(3), 781–797. https://doi.org/10.5194/amt-7-781-2014

Polissar, A. V., Hopke, P. K., Paatero, P., Malm, W. C., & Sisler, J. F. (1998). Atmospheric aerosol over Alaska—2. Elemental composition and sources. *Journal of Geophysical Research: Atmospheres*, *103*(D15), 19045–19057. https://doi.org/10.1029/98JD01212